APEC Climate Center Research Report 2017-04

Development of a Drought Forecast Model for Fiji based on High-Resolution Dynamic Downscaling of Climate Data and Machine Learning of Long-Range Climate Forecast and Remote Sensing Data

Jinyoung Rhee Strategic Planning Team

Hongwei Yang Climate Research Team

APCC
APEC CLIMATE CENTER

PREFACE

This project aims to reduce Fiji's vulnerability to droughts and help decision-makers plan for increased resiliency to droughts by providing timely and spatially detailed drought forecasting data. A drought forecast model for Fiji was developed based on high-resolution dynamic downscaling of climate data and machine learning of long-range climate forecast and remote sensing data.

This project targets national, provincial, and regional officials whose main duties include water resource and agriculture management. The final beneficiaries of the product are the residents of the area, water users, and farmers. These groups can benefit from decision making informed by drought forecast information with a finer spatial resolution.

We hope that the results and data outputs of this study can provide the application sectors with improved high-resolution climate forecast information that can eventually support the building of a long-term warning system. The end-users and policy-makers will be able to weigh their response options based on these reliable local scale projections.

APCC will continue to promote the best use of our research outcomes in various theoretical and application areas through project such as this one. Our successes and achievements would not have been possible without the support of our valued partners. In addition to my appreciation to the APCC researchers, I extend my thanks to you and hope you enjoy this research report.

Dr. **Hong-Sang Jung**
Executive Director
APEC Climate Center
March 2018

ABSTRACT

This study developed a drought forecast model for Fiji based on high-resolution dynamic downscaling and machine learning of long-range climate forecast data and remote sensing data. The downscaled dataset with 8 km resolution adequately represented the detailed temporal and spatial features of rainfall beside the add value. Bias correction further increased the reliability of the downscaled rainfall dataset. The downscaled dataset did not show clear dry trends during the past 30 years. The leeward side of Viti Levu at an elevation between 200 m and 300 m was very sensitive to SPCZ variability. The downscaled dataset effectively responded to the anomalous large-scale patterns, which provided a solid ground to develop the drought prediction model.

Drought index SPI6 was used as the target variable to indicate drought conditions. Machine learning models were trained using the drought index, which was calculated using in-situ data. There are few weather stations with available precipitation data; this provided insufficient datasets for machine learning models. Limited distribution of weather stations may also hamper examination of spatial characteristics of drought occurrences.

Bias-corrected WRF model precipitation outputs with 8 km spatial resolution were used to calculate SPI6_OBS instead of the index using in-situ data. The use of these WRF model outputs increased drought accuracy and decreased MAE for drought categories in SPI6 forecasting with shorter lead times, whether either the bias-corrected climate model outputs or machine-learning models were used.

CONTENTS

1. INTRODUCTION ---- 1
1.1 Regional Historical Droughts and Their Impacts in Fiji ---- 1
1.2 Existing Monitoring and Prediction Systems Related to Drought ---- 3
1.3 Research Questions and Objectives of the Study ---- 4

2. STUDY AREA ---- 6

3. LITERATURE REVIEW ---- 7
3.1 High-Resolution Dynamic Downscaling of Climate Data ---- 7
3.2 Drought Forecasting ---- 8

4. MATERIAL ---- 9
4.1 In-Situ Data ---- 9
4.2 SPI ---- 9
4.3 Reanalysis Data ---- 9
4.4 Seasonal Forecast Data ---- 10
4.5 Remote Sensing Data ---- 10

4.5.1 CMORPH Data 10
4.5.2 PERSIANN-CDR 10
4.5.3 TRMM 11
4.5.4 GPM 11
4.5.5 MODIS Land Surface Temperature 11
4.5.6 MODIS Vegetation Indices 12
4.5.7 Elevation Data 12
4.6 SPCZ 13
4.7 ENSO 14
4.8 PDO 14

5. METHODOLOGY 16
5.1 High-Resolution Dynamic Downscaling of Climate Data 16
5.2 Drought Forecasting 19
5.2.1 Machine Learning Models 19
5.2.2 Preprocessing of Input Variables 20
5.2.3 Performance Measures 20

6. RESULTS 22
6.1 Impact of Large-Scale Modes on Wet and Dry Conditions over Fiji 22
6.1.1 Observed Rainfall Features and SPI 22
6.1.2 Composite of Observed Wet and Dry Events 23
6.2 Production of 8km WRF Model Outputs 25
6.2.1 Regional Simulation of Climatology over Fiji 25
6.2.2 Temporal Evolution of Rainfall 27
6.2.3 Spatial and Temporal Distribution of SPI 27

6.2.4 Composite Analysis of Simulated Wet and Dry Events ---- 28
6.3 Bias Correction ---- 29
6.4 Development of a Drought Forecast Model ---- 29
6.4.1 SPI6 Forecast Based on Bias-Corrected Climate Models (FCST_ONLY) ---- 29
6.4.2 SPI6 Forecast Based on Machine Learning Models ---- 31
6.5 Validation of the Drought Forecast Model ---- 31

7. CONCLUSION ---- 33

Appendix A. Guideline for the Application of the Drought Forecast Model ---- 35
A.1 Select a Drought Index ---- 35
A.2 Select Performance Measures ---- 35
A.3 Select a Method and Climate Model ---- 35
A.4 Create Spatially Distributed SPI6 Forecast Maps ---- 36
A.5 Create Zonal Average Maps ---- 36

Acknowledgements ---- 36

REFERENCES ---- 37

TABLES ---- 43

FIGURES ---- 46

1. INTRODUCTION

1.1 Regional Historical Droughts and Their Impacts in Fiji

Islands in the South Pacific are vulnerable to climate change (Solomon 2007). Hay et al. (2003) showed that the climate in the South Pacific has become drier and warmer by 15% and 0.8 °C, respectively, compared to earlier in the 20th century. Fiji, one of the key Pacific Island countries, experiences easterly trade winds on most calendar days. The easterly trade winds or the northeasterly monsoon, when lifted by high mountains, causes moisture condensation and produces heavy rainfall on the windward eastern side of Fiji. The subsidence of the relatively dry air produces less rainfall on the leeward western side.

From a large-scale viewpoint, the El Nino Southern Oscillation (ENSO) is the main cause of climate variability over this region at interannual timescales. La Nina events dominated the interannual sea surface temperature anomaly (SSTA) over the central Equatorial Pacific during 1950 and 1975; after that time El Nino events became more frequent (Trenberth and Hoar 1996). The Pacific Decadal Oscillation (PDO) dominates the climate variability at decadal timescales (Mantua et al. 1997). PDO was mostly positive prior to 1998 and then shifted to a strong negative phase (Mantua and Hare 2002). Positive PDO is characterized by the similar SSTA of El Nino over the Equatorial Pacific, and thus shifts the weather systems northeastward, but on a decadal timescale. The South Pacific Convergence Zone (SPCZ) is a reverse-oriented monsoon trough with strong low-level convergence and a rainfall band that extends from the Warm Pool southeastward to French Polynesia (Bergeron 1930; Trenberth 1976). The interferential impact of ENSO and PDO on the SPCZ is complex (Folland et al. 2002; Hu and Huang 2009). El Nino events weaken the strength of the Walker Circulation and shift the dominant weather systems over the Equatorial Pacific toward areas in the northeast such as the SPCZ. When El Nino takes place during the positive PDO, the SPCZ moves northeast toward the equator and its intensity becomes stronger (Folland et al. 2002). The large-scale convection departure decreases precipitation over Fiji and leads to droughts (Nicholls and Wong 1990).

Fiji has observed more frequent dry conditions since the 1950's compared to previous decades in the Western and Northern areas based on analysis performed using the Standardized Precipitation Index (SPI). Analysis of observed monthly rainfall for Fiji over the period 1949-2008 showed downward trends at a 99% confidence level with decreases in rainfall of approximately 13 mm - 47 mm per year (Deo 2011). Although no significant long-term trends were observed in annual rainfall (Mataki et al. 2006), there were more frequent dry seasons during the last 50 years compared to the first 50 years in this period (Kumar et al. 2014). The local temperature also increased due to the effects of climate change (Kumar et al. 2013). The most impacted stations were located in western and northern Fiji, where deficiency in rainfall from 1969-1988 caused an increase in moderate and severe droughts (Deo 2011). In the future, Risbey et al. (2002) projected an increase in rainfall of approximately 3.3% by 2025 and 9.7% by 2100 using a global climate model (GCM). Feresi et al. (2000) and Agrawala et al. (2003) did not project a definitive change in rainfall. Stocker (2014) projected that Fiji will experience an intensified seasonal cycle, i.e., a rainfall decrease in the dry season and a rainfall increase in the wet season. The shift towards extended periods of dry spells causes loss of soil fertility, which could impact negatively on agriculture (Solomon 2007).

Since 1940, severe droughts have occurred in 1942, 1958, 1969, 1978, 1983, 1987, 1992, 1997-1998, 2003, and 2010 (Feresi et al. 2000). Severe droughts can cause serious socio-economic loss as well as physical damages as drought conditions persist. The ENSO event of 1997-1998 caused a severe drought with damages of up to Fiji$100 million. Rainfall failure occurred across two successive dry seasons, and, more significantly, during the intervening wet season when precipitation is normally reliable (Feresi et al. 2000). Since many rural communities are reliant on rainwater, streams, and shallow wells for domestic use, watering crop gardens, and livestock, these communities are especially vulnerable to periods of drought when surface water resources are at a minimum (Terry and Raj 1999). Schools and businesses were forced to close and caused disruption to residential areas. Such impacts made extreme difficulties for Fiji since the resources of an island country are limited. External aid and governmental assistance were required to ensure supply of sustenance and facilitate recovery in the worst-hit parts of Fiji, which included the western and northern divisions and outer islands.

1.2 Existing Monitoring and Prediction Systems Related to Drought

The SPI described in detail in Section 4.2 is used for drought monitoring in Fiji. SPI values for drought prediction are calculated based on the statistically downscaled seasonal forecast data from the Seasonal Climate Outlooks for Pacific Island Countries developed by the Bureau of Meteorology of Australia.

The monitoring network over Fiji is very sparse, resulting in considerable uncertainty in the estimates of extreme wet and dry events. Evidence shows that estimation of the historical trends has a large noise-to-signal ratio over regions with sparse data networks (Yin et al. 2015). Most Fiji weather stations are located along the coastline, so the sparse network cannot capture small-scale convective precipitation over land and precipitation from orographic lifting at mountains. Furthermore, rainfall variability in the high mountains is greater than the variability in cities.

The limited variables and inconsistency in duration of satellite observation introduces difficulties and uncertainties in methods and analysis For example, the Climate Prediction Center Morphing Technique (CMORPH) data is only available from 1998 onward. Due to the limited number or variables being observed, it is difficult to prepare for droughts because the response of rainfall distribution to large-scale dynamics is unclear. In addition, unlike other types of disasters, the onset and termination of droughts is not always clear. The increase in uncertainty of climate variability makes the reduction of drought impacts even more difficult.

This research attempts to build a drought forecast system based on the historical dataset using high resolution dynamic downscaling and multi-sensor remote sensing data.

For an island characterized by high mountains surrounded by ocean with complex coastlines, dynamic downscaling using a regional climate model can provide a full dataset including frequent hydrological output with high spatial resolution. The global climate model generally has low horizontal resolution (~100 km) and cannot represent regional to local details and underlying physical sub-grid scale processes that may cause extreme events (Rummukainen 2010). The high-resolution distribution of hydrological variables obtained by dynamic downscaling can complement the shortage of observations over Fiji, either on few stations on spatial or the missing data. This forecast system is relatively reliable since the regional climate model with spectral nudging can only adopt the large-scale signals from the reanalysis data. The physical-dynamical consistency of many variables in dynamic downscaling can supplement satellite observations to be used as reference data in the drought forecast model.

Drought conditions in Fiji are currently monitored using the 3-, 6-, and 12-month SPI (http://www.met.gov.fj/ENSO_Update.pdf). Drought forecasting for the SPI or other target variables related to drought can be useful in preventing and minimizing the adverse impacts of droughts. This project seeks to obtain high-resolution drought forecasting data for Fiji. Climate and long-range forecast data are used to estimate the effect of synoptic and large-scale atmospheric circulation, such as that in the SPCZ which is modulated by ENSO and PDO, that result in droughts in Fiji (Kumar et al. 2014). Severe droughts can cause huge socio-economic loss. Thus, it is a priority to build a drought forecast system that can provide real-time drought information under high resolution. Taking advantage of the high resolution dynamically downscaled data and the multi-sensor remote sensing data, the forecast system will be able to reflect regional characteristics and provide effective long-leading forecast information.

1.3 Research Questions and Objectives of the Study

This project aims to reduce Fiji's vulnerability to droughts and help decision makers plan for increased resiliency to droughts by providing timely and spatially detailed drought forecasting data for the area. Drought index values calculated for weather stations or obtained based on low-resolution bias-corrected seasonal forecast data are not sufficient. Machine learning can help to provide spatially distributed drought information. High-resolution dynamic downscaling enables the provision of sufficient data for training of machine learning models.

Objectives of this study are to: (1) produce high-resolution dynamically downscaled climate data for Fiji; (2) develop a drought forecast system based on machine learning of long-range climate forecast and remote sensing data.

This project targets national, provincial, and regional officials whose main duties include water resources and agricultural management. The final beneficiaries of the product are residents of the area; water users and farmers for whom decision-making can be helped by drought forecast information with finer spatial resolution.

2. STUDY AREA

Fiji has a total area of about 194,000 km^2 of which approximately 10% is land. Fiji consists of 332 islands. The two largest islands are Viti Levu and Vanua Levu, which account for about three-quarters of the total land area of Fiji (Derrick 1957). Figure 1 shows the topography of Fiji's main islands. The largest island, Viti Levu, which has an area of 10,388 km^2, is covered with thick tropical forest. The island has a considerable area higher than 500 m in elevation with the peak of Mount Tomanivi at 1,324 m above sea level. Viti Levu hosts the capital city of Suva, which contains about three-quarters of the population. Other important towns include Nadi, where the international airport is located, and Lautoka.

Sugar export is an import source of foreign exchange for Fiji, as sugar cane processing makes up one-third of industrial activity. Coconuts, ginger, and copra are also significant industries. These agriculture products are highly influenced by climate extremes; the sugar industry was damaged by drought in 1998.

Fiji has a tropical marine climate and is warm year-round with minimal extremes. The warm season lasts from November to April and the cool season lasts from May to October.

Temperatures in the cool season average 22 °C. Winds are moderate, though cyclones occur about once a year (10-12 times per decade). Viti Levu is a mountainous volcanic island with a wet-dry tropical climate. The southeast side of the island faces the predominant trade winds and therefore receives more precipitation than the northwest side, which is rain-shadowed by interior highlands. The volcanic mountains force orographic lifting of the saturated air, which can produce extremely heavy rainfall on the windward side of the mountain. Rainfall on the leeward side is much lighter due to the subsidence of the dry air, which largely influences agriculture in those areas. In the dry season, the uneven distribution of rainfall can cause a prolonged lack of moisture on the leeward side. The leeward side only receives 20% of the annual total rainfall in the dry season, compared to 33% received on the windward side (Terry and Raj 1998).

3. LITERATURE REVIEW

3.1 High-Resolution Dynamic Downscaling of Climate Data

The Fiji islands have high mountains surrounded by ocean and complex coastlines. Dynamic downscaling using a regional climate model can provide a full dataset including frequent hydrological output with high spatial resolution. Yang (2013, 2015) carried out dynamic downscaling research over the Maritime Continent (MC) at both 50 km and 25 km spatial resolutions. The experiment applying the 25 km grid outperformed the experiment applying the 50 km grid for many factors such as added value, spatial and temporal correlation, and root-mean-square error. The added value is attributed to the increase of the resolution. Viti Levu, Fiji's largest island, has an area of 10,389 km^2. There will only be 16 grids over the research area if the 25 km grid resolution is used, which is not enough to distinguish the characteristics of the underlying surface.

Using the European Centre for Medium-Range Weather Forecasts Reanalysis (ERA) Interim reanalysis dataset under 0.75°horizontal resolution, multiple nested domain is necessary to carry out the dynamic downscaling to a scale smaller than 25 km. This would fall into the so-called "gray zone" resolution, typically 1 km to 15 km resolution in which the deep convection is partly resolved and partly sub-grid (Gerard 2007). The critical grid scale for convection parameterization, and the strengths and weaknesses of dynamic downscaling at "gray zone" resolution, are active research areas (Lal et al. 2008; Yu and Lee 2010; Jung et al. 2012; Wang et al. 2015)

Lal et al. (2008) carried out a climate simulation at 8 km resolution over Fiji using a global variable-resolution model initiated with reanalysis nudging, which was the first climate simulation over Fiji at such a scale. Results showed that the model could realistically simulate the annual cycle, intra-seasonal variation, and interannual variability of rainfall, as well as the response of rainfall to El Nino. Chattopadhyay and Katzfey (2015) used the same model to simulate the climate of Fiji and the Federated States of Micronesia with a two-step, one-way nest strategy (60 km then 8 km) following the Coupled Model Intercomparison

Project Phase 3 models. Their results show that the 8 km simulations are capable of realistically depicting the current climate when topography influences wind flow and rainfall, which is the case for Fiji.

3.2 Drought Forecasting

Mishra and Singh (2011) reviewed a variety of drought modeling methods and described the components of drought modeling as hydro-meteorological variables, drought indices, climate indices, methodologies, and outputs (Figure 2). Among hydro-meteorological variables, rainfall is the most important variable for meteorological drought forecasting, soil moisture and crop yield are the key variables for agricultural drought forecasting, and stream flow and reservoir level are the most important variables for hydrological drought forecasting. Sometimes many variables are combined to obtain drought characteristics such as drought severity, duration, and spatial extent. Large-scale climate indices such as ENSO or the Arctic Oscillation (AO) index are used to forecast longer droughts. There can be many methods used including regression models, time-series models, probability models, and neural networks models (Leilah and Al-Khateeb 2005; Steinemann 2006; Morid et al. 2007; Han et al. 2010; Mishra and Singh 2011) (Figure 2).

Recently, drought-forecasting methods using machine learning have been developed (Tadesse et al. 2005; Rhee and Im 2017). Rules required by expert systems can be developed either by human experts or derived by machines based on data provided by human beings; this training process is called machine learning (Jensen and Lulla 1987). Tadesse et al. (2005) developed a rule-based regression tree model forecasting drought conditions and crop yield based on remotely sensed vegetation conditions, SPI, land use, available water capacity of soil, and irrigation areas. Rhee and Im (2017) tested decision tree models, random forest models, and extremely randomized tree models to forecast drought indices of the SPI and the Standardized Precipitation-Evapotranspiration Index in South Korea.

4. MATERIAL

4.1 In-Situ Data

Figure 3 shows the location of rainfall gauges used in this report. Gauge names and coordinates are shown in Table 1. The gauges provided valid data from 1981 to 2010 with the exception of missing data during a short period of time from gauges at Udu Point and Nabouwalu.

4.2 SPI

The SPI is widely used to characterize meteorological drought on a range of timescales (Guttman 1999; McKee et al. 1993). It quantifies observed precipitation as a standardized departure from a selected probability distribution function that models the raw precipitation data. The raw precipitation data are fitted to a gamma distribution and then transformed to a normal distribution. The SPI values can be interpreted as the number of standard deviations by which the observed anomaly deviates from the long-term mean. The SPI can be created for differing periods of 1 to 36 months, using monthly input data. The SPI can be compared across regions with markedly different climates.

4.3 Reanalysis Data

In this study, we use the ERA-Interim as the large-scale forcing data to drive the Weather Research and Forecast (WRF) model (Dee et al. 2011). The ERA-Interim is a second-generation atmospheric reanalysis product created by the European Centre for Medium-Range Weather Forecasts (ECMWF). The ERA-Interim data are available at 6-h intervals with a horizontal resolution of 0.75°and 37 pressure levels. The dataset spans the period from 1979 to the present. The ERA-Interim product has made many improvements in the depiction of atmospheric circulation and boundary layer processes compared to the previous generation of reanalysis products.

4.4 Seasonal Forecast Data

Seasonal forecast data from seven individual climate models, including the Asia-Pacific Economic Cooperation Climate Center (APCC) Multi-Model Ensemble (MME), producing precipitation forecasts up to 6 months were used in this study. Only the MME data with the Simple Composite Method were used. The individual climate models used were APCC, the Centro Euro-Mediterraneo sui Cambiamenti Climatici, the Meteorological Service of Canada (MSC), the National Aeronautics and Space Administration (NASA), the National Centers for Environmental Prediction (NCEP), Pusan National University (PNU), and the Predictive Ocean Atmosphere Model for Australia (POAMA) models.

4.5 Remote Sensing Data

4.5.1 CMORPH Data

Satellite rainfall data from CMORPH consists of half-hourly measurements on an 8 km grid, and data is available from 1998 onward (Joyce et al. 2004). AghaKouchak et al. (2011) showed that CMORPH is capable of detecting extreme precipitation events.

4.5.2 PERSIANN-CDR

The drought forecast model developed in this study relies on remote sensing based precipitation data in order to compensate for the low spatial coverage of weather stations. To secure precipitation data covering a large enough area, the Precipitation Estimation from Remotely Sensed Information using Artificial Neural Networks (PERSIANN)-Climate Data Record (CDR) was used (Ashouri et al. 2015). PERSIANN-CDR data were created based on infrared sensor data for the period with no microwave sensor data. The data cover 60 °S – 60 °N, 180 °W – 180 °E, with a spatial resolution of 0.25°× 0.25°. Daily data were obtained and converted to monthly total precipitation data.

4.5.3 TRMM

The tropical rainfall measuring mission (TRMM) was developed jointly by the United States (US) NASA and the Japan Aerospace Exploration Agency. The TRMM 3B42 product with 3-h data collection intervals was obtained from the US Goddard Earth Sciences Data and Information Service Center (GES DISC) and converted to monthly total precipitation data. The TRMM data cover 50 °S – 50 °N, 180 °W – 180 °E, and have a spatial resolution of 0.25°× 0.25°. The data are in Equirectangular (or geographic) projection with WGS84 datum.

4.5.4 GPM

The Integrated Multi-Satellite Retrievals for the Global Precipitation Measurement Mission (GPM) data were used as remote sensing based precipitation data from April 2014 onward. The data were obtained from the Precipitation Measurement Missions of NASA (http://pmm.nasa.gov/data-access/downloads/gpm), and cover 90 °S – 90 °N, 180 °W – 180 °E, and have a spatial resolution of 0.1°× 0.1°. The data are also in Equirectangular (or geographic) projection with WGS84 datum. The data were converted to monthly total precipitation data.

4.5.5 MODIS Land Surface Temperature

Daytime and nighttime land surface temperature (LST) data from the Level-3 standard product of the Moderate Resolution Imaging Spectroradiometer (MODIS) onboard the Aqua satellite, MYD11A2 LST and Emissivity 8-day L3 Global 1km, were obtained from the Earth Observing System Data and Information System EARTHDATA (https://earthdata.nasa.gov) of NASA from July 2002 to December 2016. MYD11A2 data are the average of daily MYD11A1 data of cloud-free days. Temporal and spatial resolutions of the data are 8-days and approximately 1 km × 1 km, respectively. The data are projected in Sinusoidal projection.

Since the time scale of the developed drought forecast model is monthly, the 8-day data were converted into monthly data using the number of days of the 8-day period for each month as weights. Mean LST (LST_MEAN) was also calculated from daytime LST (LST_DAY) and nighttime LST (LST_NIGHT).

4.5.6 MODIS Vegetation Indices

Vegetation indices of the Normalized Difference Vegetation Index (NDVI) and the Enhanced Vegetation Index (EVI) were obtained from the Level-3 data of MODIS onboard Aqua, MYD13A3 Vegetation Indices Monthly L3 Global 1km, from EARTHDATA of NASA from July 2002 to December 2016. Temporal and spatial resolutions are monthly and approximately 1 km x 1 km, respectively. The data are also projected in Sinusoidal projection.

The NDVI (equation (1)) can be calculated using the changes in reflectance in red and Near Infrared (NIR) channels, and has been widely used as an indicator of vegetation vigor (Tucker 1979). The EVI uses the blue band in addition to red and NIR bands, minimizing the influence of the background effect of soil, snow, and water. The EVI retains sensitivity to vegetation vitality, which is often shown saturated in the NDVI. The blue band helps to remove the atmospheric effect caused by air and clouds.

$$NDVI = \frac{NIR - RED}{NIR + RED}$$

$$EVI = 2 \times \frac{NIR - RED}{L + NIR + C1 \times RED + C2 \times BLUE}$$

where NIR, RED, and $BLUE$ are reflectance values of NIR, red, and blue channels, respectively; L is a parameter for reducing the background effect of canopy; $C1$ and $C2$ are weighting parameters to correct the influence of the aerosol effect of the red band when the blue and red bands are used together (Liu and Huete 1995).

4.5.7 Elevation Data

Global 30 Arc-Second Elevation (GTOPO30) data with 1 km × 1 km spatial resolution were obtained from the US Geological Survey and used for the study area.

4.6 SPCZ

The SPCZ, a reverse-oriented monsoon trough, is a band of low-level convergence, cloudiness, and precipitation extending from the Western Pacific Warm Pool at the maritime continent southeastward toward French Polynesia and as far as the Cook Islands (160 °W, 20 °S). The SPCZ occurs where the southeast trade winds from transitory anticyclones to the south meet with the semi-permanent easterly flow from the eastern South Pacific anticyclone.

To study the SPCZ and its impacts on weather and climate over the South Pacific islands, previous studies suggested several SPCZ indices (Borlace et al. 2014; Cai et al. 2012; Folland et al. 2002; Kidwell et al. 2016; Vincent et al. 2011). Here we adopted the SPCZ strength index from Kidwell et al. (2016) to quantitatively study the impact of the SPCZ on rainfall over Fiji. The SPCZ region was encompassed in 0 °S – 30 °S, 130 °E – 110 °W. The strength of the SPCZ is defined by the surface wind convergence in this region derived from the ERA-Interim. Divergence was calculated with the following:

$$D(x,y)=\frac{\partial u}{\partial x}+\frac{\partial v}{\partial y}$$

where and are the zonal and meridional components of the surface winds, positive corresponds to surface divergence, and a negative D corresponds to surface convergence. The SPCZ strength is defined by the monthly mean area-weighted average value of convergence within the SPCZ region:

$$s=\sum D(x,y)a(x,y)/\sum a(x,y)$$

where $a(x,y)$ is the area of a grid cell centered at location (x,y), and the spatial summation $\sum$ is performed over grid cells with $D(x,y)<0$ within the SPCZ region. The anomaly of the SPCZ strength is defined as SPCZ index. Figure 9 shows the monthly SPCZ index derived from the ERA-Interim. The SPCZ index shows strong events in 1983 and 1998.

4.7 ENSO

The ENSO is an irregularly periodic variation in winds and SST over the tropical eastern Pacific Ocean, affecting much of the tropics and subtropics. The warming phase is known as El Nino and the cooling phase as La Nina. Southern Oscillation is the accompanying atmospheric component, coupled with the sea temperature change; El Nino is accompanied with high, and La Nina with low air surface pressure in the tropical western Pacific. The two periods last several months each (typically occurring every few years) and their effects vary in intensity.

The Oceanic Nino Index (ONI), constructed from the National Oceanic and Atmospheric Administration (NOAA) extended reconstructed SST data, was used to measure the warm and cold interannual events in the pacific (Huang et al. 2015), Figure 11 shows the ONI defined as the 3-month running mean of SSTA in the Nino 3.4 region. The SST climatology is calculated from 1940 to 2010. Trenberth (1976) described the movement of the SPCZ as north and east during El Nino events and south and west during La Nina events.

4.8 PDO

The PDO is a robust, recurring pattern of ocean-atmosphere climate variability centered over the mid-latitude Pacific Basin (Mantua et al. 1997). The PDO is detected as warm or cool surface waters in the Pacific Ocean, north of 20 °N. Over the past century, the amplitude of this climate pattern has varied irregularly at interannual to interdecadal time scales (meaning time periods of a few years to as much as time periods of multiple decades). The PDO index is defined by the leading empirical orthogonal function (EOF) pattern of SST anomalies in the North Pacific Basin (typically poleward of 20 °N). The SSTA are obtained by removing both the climatological annual cycle and the global-mean SST anomaly from the data at each grid point. Positive values of the PDO index correspond with negative SST anomalies in the central and western North Pacific (extending eastward from Japan), and positive SST anomalies in the eastern North Pacific (along the west coast of North America). Figure 12 shows the normalized PDO index calculated from extended reconstructed SST (ERSST) based on the climatology during 1940 to 2010. Before 1998, the PDO was mostly positive. From 1999 onward, the PDO has mostly been strongly negative.

When ENSO and PDO are in (out) phase, weaker/stronger trade winds in the tropical Pacific coupled to warmer/colder SST in the eastern-central Equatorial Pacific increase (decrease) their magnitude. This is an important factor in the longitudinal position of the SPCZ.

5. METHODOLOGY

5.1 High-Resolution Dynamic Downscaling of Climate Data

In this study the WRF Model version 3.5, which is a primitive equation limited-area model under sigma coordinates, was used as the dynamic downscaling tool. In general, WRF is a regional prediction and downscaling system designed to meet both operational forecasting and atmospheric research needs. This system has advanced software architecture that allows for parallel computing and system extensibility. The development of state-of-the-art WRF technology was undertaken as a collaborative project by several organizations including the National Center for Atmospheric Research (NCAR), the Forecast Systems Laboratory, NOAA, NCEP, the Air Force Weather Agency (AFWA), the Naval Research Laboratory, the University of Oklahoma, and the Federal Aviation Administration. The WRF model allows researchers to conduct simulations reflecting either real data or idealized configurations. WRF is suitable for many applications at different scales ranging from meters to thousands of kilometers. Such applications include research and operational numerical weather prediction, data assimilation and parameterized physics research, downscaling climate simulations, driving air quality models, atmosphere-ocean coupling, and idealized simulations of phenomenon such as boundary layer eddies, convection, and baroclinic waves. There are two dynamics solvers in the WRF Software Framework, namely, the Advanced Research WRF (ARW) solver (originally referred to as the Eulerian mass or "em" solver), which was developed primarily at NCAR, and the Nonhydrostatic Mesoscale Model solver, which was developed at NCEP. We employed the ARW solver in this study. The governing equations of the ARW dynamics solver are the compressible, nonhydrostatic Euler equations. These equations are written in flux form and their variables satisfy conservation equations following the philosophy of Ooyama (1990). Further, the equations are expressed by using a terrain-following mass vertical coordinate system (Laprise 1992). In this model, the top surface is a constant pressure surface; we set this surface at a pressure of 50 hPa. Arakawa C-grid staggering was applied for the horizontal grid. A third-order Runge Kutta scheme with a smaller time step for acoustic and gravity-wave modes was applied for time-split integration (Klemp and Wilhelmson 1978; Skamarock and Klemp 1992; Wicker and Skamarock 2002). The WRF model offers multiple physical options that can be combined in any way (Skamarock et al. 2005).

The model domain focused on the main islands of Fiji, Viti Levu and Vanua Levu (Figure 1). Double nested domain was used to simulate the Fiji islands in order to resolve issues of the complex coastline and high topography (Figure 4). The mother domain was in 25 km resolution and the corresponding experiment utilized the spectra technique to ensure a reliable forcing was available to drive the 8 km resolution domain. We named the experiment at a resolution of 8 km as WRF_8km. Experiment WRF_8km took the output from the experiment in 25 km resolution as the lateral boundary forcing and did not use spectral nudging. The 8 km resolution is the finest resolution that would generally be used with a hydrostatic model in areas with deep convection.

To consider the climate system in this region, we needed: (1) a sufficiently large domain size so that the regional model could develop its own dynamics; (2) sufficient computational resources. The mother domain covering the Fiji region extended from 31.5 °S – 3 °S and from 160 °E – 196 °E, and the nested domain extended from 21.5 °S – 13 °S and from 173 °E – 184 °E (Figure 4). We chose the cylindrical equidistant map projection because the grid is almost rectangular in Euclid space over the tropical region. Our target period was the most recent 30 years from 1981 to 2010. Observed rainfall from rain gauge stations and CMORPH rainfall (8 km) were used to verify the model result.

For the mother domain experiment at 25 km resolution, we chose the WRF Single-Moment 6-Class Microphysics graupel scheme (Hong et al. 2004) for microphysics parameterization; this scheme includes six types of hydrometeors, namely, water vapor, cloud water, rain, cloud ice, snow, and graupel in six different arrays. The scheme accounts for the existence of supercooled water and gradual melting of snow below the melting layer. It introduced a new method for representing mixed-phase particle fall speeds weighted by the mixing ratios for the snow and graupel particles by assigning a single fall speed to both; this fall speed was applied to both sedimentation and accretion processes. We chose the Kain-Fritsch (new Eta) scheme for cumulus parameterization; this is a deep and shallow convection sub-grid scheme that uses a mass flux approach with downdraft and convective available potential energy removal time scales (Kain 2004; Kain and Fritsch 1990). The long wave and short wave radiative transfer model followed the Community Atmospheric Model (CAM) scheme, which is based on the CAM 3 climate model used in the Community Climate System Model (Collins et al. 2004). Land-surface parameterization follows the unified Noah land-surface model, which is a unified NCEP/NCAR/AFWA scheme that describes soil temperature and moisture in four layers, fractional snow cover, and frozen soil physics (Tewari et al. 2004). The Yonsei University boundary layer (PBL) was employed here; with this technique, the counter gradient terms were used to represent fluxes due to non-local gradients (Hong et al. 2006). The surface layer scheme used was the Fifth-Generation Penn State/NCAR Mesoscale Model Monin-Obukhov scheme, which is based on the Monin-Obukhov scheme with a Carlson-Boland viscous sub-layer and standard similarity functions to look-up tables (Beljaars 1995; Dyer and Hicks 1970; Paulson 1970; Webb 1970; Zhang and Anthes 1982).

For the nested domain experiment in 8 km resolution, we chose the Thompson scheme for microphysics parameterization; this scheme includes ice, snow and graupel processes suitable for high-resolution simulations (Thompson et al. 2008). We chose the Grell-Freitas ensemble scheme for cumulus parameterization; this scheme is an improved Grell-Devenyi scheme that smoothes the transition to cloud-resolving scales (Arakawa 2004). The long wave and short wave radiative transfer model used was the rapid radiative transfer model for GCMs (RRTMG) scheme (Iacono et al. 2008). The RRTMG model allows for multiple choices in various settings, such as different cloud overlap assumptions and ice cloud optical properties parameterization schemes. The choice of land surface parameterization, PBL scheme, and surface layer scheme were the same as in the experiment of for the mother domain experiment.

The lateral boundary forcing fields included geopotential height, air temperature, specific humidity, and horizontal winds. The width of the buffer zone in our model was set at 10 grid points. The prognostic variables of the WRF model were nudged toward the large-scale forcing fields following the method of Davies and Turner (1977) with Newtonian nudging and horizontal diffusion within the regional climate model buffer zones. The initial state conditions measured were surface pressure, sea-level pressure, 2-m height moisture, 2-m height temperature, 10-m height horizontal winds, soil moisture, soil temperature, and skin temperature. The skin temperature over the ocean was considered the SST. We obtained 10-m horizontal resolution topography and land use data for the Noah land surface model from the U.S. Geological Survey. The 10-m resolution soil type data were obtained from the State Soil Geographic Database, and the 10-m resolution global data were obtained from the Food and Agriculture Organization of the United Nations.

5.2 Drought Forecasting

5.2.1 Machine Learning Models

The Extremely Randomized Trees (ERT) and the Adaboost models were used as the machine learning models for this study. ERT is known to produce stable results against outliers and noise in training data, and had excellent performance in drought forecasting (Rhee and Im 2017). Adaboost is a weak learner; it enables the model to simulate minor characteristics of training data by assigning higher weights to the subsets that are less reflected during its iteration processes.

ERT and Adaboost models have several input variables and a target variable. Input variables include month of the data (MONTH), LST_DAY, LST_NIGHT, LST_MEAN, NDVI, EVI, elevation (ELEV), SPI6_FCST (SPI6 calculated from precipitation data combining seasonal forecasted rainfall and remote sensing based rainfall), the Multivariate ENSO Index (MEI) (which is one of the ENSO indices), and SPCZ (SPCZ strength). The target variable is SPI6_OBS based on observational data. The Fiji Meteorological Service (FMS) uses SPI6 to examine agricultural (soil moisture) and hydrological drought because the 6-month droughts affect deeper rooted plants and medium-sized water bodies (FMS, personal communication).

A time-series of reference data for the target variable was used to train the models along with data for input variables (Figure 5). Machine learning models for each month were developed separately.

In this study, two cases were compared; in one case, training and testing (final evaluation) were performed at six weather station locations (SPI6_OBS were calculated based on in-situ data). In the other case, training and testing were performed at the 227 pixel locations of WRF model outputs (SPI6_OBS were calculated based on WRF model outputs). Spatially distributed drought forecast information of SPI6 was produced for Fiji from the selected drought forecast model.

5.2.2 Preprocessing of Input Variables

Preprocessing was not required for variables of MONTH, MEI, and SPCZ. Remote sensing based variables of LST_DAY, LST_NIGHT, LST_MEAN, NDVI, EVI and ELEV were all subset to the extent of 176.5 °E – 178 °W, 21.5 °S – 12.0 °S and then resampled to have 0.01° × 0.01°spatial resolution. Since many machine learning models tend to be sensitive to the magnitudes of input variables, these data were scaled using maximum and minimum values of each month for each pixel (Rhee et al. 2010).

For SPI6_FCST, seasonal forecast data were bias-corrected using percent increment of anomaly and monthly climatology of remote sensing based precipitation data (Quan et al. 2012). SPI6_RS, remote sensing based SPI6, was used to train the ERT and Adaboost models, and SPI6_FCST was used for validation and testing.

Since SPI is inherently Gaussian, numbers of input data sets for each drought category, or any defined categories with equal intervals, are not even. Additional input data were created with added noise by multiplying the standard deviation of the variable for the location and month with a random number between 0 and 1, so that all categories had the same sample numbers during training. This process was included because some machine learning models are sensitive to the number of samples producing a certain range of values for the target variable.

5.2.3 Performance Measures

Information on drought index values or drought categories indicating the severity of drought can be more useful to users than just having binary information of drought or non-drought. Two performance measures were used in this study: Drought Accuracy, which was defined as a modified producer's accuracy in Rhee and Im (2017), and mean absolute error (MAE) of drought categories including moderate, severe, and extreme drought.

$$Drought\ \ Accuracy = \frac{C_{ED}+C_{SD}+C_{MD}}{N_{ED}+N_{SD}+N_{MD}}$$

$$MAE = \frac{\sum|SPI6_{obs}-SPI6_{pred}|}{Total\ \ Nmber\ \ of\ \ Samples}$$

where ED, SD, MD and are drought categories for Extreme Drought, Severe Drought, and Moderate Drought, respectively. Drought categories suggested by McKee et al. (1993) were used. N is the number of samples for each category, and is the number of correctly categorized samples for each category.

Due to the short history of MODIS, the period of input data from 2002 to 2016 is relatively short. There is a possibility that drought events with various magnitudes of severity may not be included in both datasets for training and testing. Thus, we adopted a 3-level procedure of training, validation, and testing. Combinations of the location, year, and month were shuffled and divided into ten groups. Seven groups were assigned for training, and three groups were solely used for testing (final evaluation). During training, leave-one-out cross-validation was performed: among the seven groups, one group was left out for validation while six groups were used for training. The average values of performance measures of these seven cases were used to select hyper-parameters of the models and to choose the best model. Hyper-parameters included the number of trees for both ERT and Adaboost models, and the maximum depth of tree growth for ERT.

6. RESULTS

6.1 Impact of Large-Scale Modes on Wet and Dry Conditions over Fiji

6.1.1 Observed Rainfall Features and SPI

Figure 6 shows the monthly rainfall time series at 4 gauges, i.e., Udu point, Nabouwalu, Nadi, and Suva. These 4 rainfall series had similar magnitudes below 30 mm/d in most months. They generally revealed the annual cycles feature. Figure 7 exhibits the observed rainfall climatological annual cycle. The rainfall at these 4 gauges clearly revealed consistent phases in the annual cycles, i.e., dry season in local winter and wet season in local summer. The annual cycles had a similar magnitude around 10 mm/d. February had less rainfall than January and March in the local summer, while July had minimal rainfall of less than 5 mm/d in the local dry winter.

The SPI is widely used to characterize meteorological drought. The green curves in Figure 8 show the observed 5-month SPI derived from the gauge rainfall at the 4 weather stations. The SPI at Udu point indicated the drought conditions in 1983, 1987, and 1998. Including those 3 years, the SPI in Nabouwalu also revealed the drought event in 1992. In Nadi and Suva, the SPIs clearly showed that drought events happened at the same time as at Udu point. Apart from exhibiting that several dry seasons took place, a clear dry trend could not be found from the gauge records for the recent 30 years from 1981 to 2010.

The SPIs at the 4 weather station locations had consistent temporal variability (Figure 10a), as the correlation coefficients between Udu Point and Suva, Nadi, and Nabouwalu were 0.47, 0.43, and 0.53, respectively. Thus, the averaged SPI (Figure 10b) could reflect the general wet and dry situations over Viti Levu and Vanua Levu. The averaged SPI showed that strong, long-lasting dry conditions occurred in 1983, 1987, and 1998, and strong, long-lasting wet conditions occurred in 1986, 1999/2000, and 2007/2008.

6.1.2 Composite of Observed Wet and Dry Events

Figure 13 shows the distribution of wet and dry events in Fiji as a function of ENSO and PDO indices conditional on the strong and weak modes of the SPCZ. When the SPCZ was strong, a total of 57 five-month wet events and 94 five-month dry events happened over Fiji (Figure 13a, b). When the SPCZ was weak, a total of 130 five-month wet events and 79 five-month dry events occurred (Figure 13c, d). It was indicated that strong SPCZ modes cause dry events and weak SPCZ modes cause wet events.

When the SPCZ was strong, 25 out of 57 wet events took place when both the ENSO and PDO were in negative phases (Figure 13a). When the ENSO and PDO were out of phase, the large-scale system did not frequently generate wet events.

Figure 13b presents 94 Fiji dry events when the SPCZ was strong. The driest events (44) happened when the ENSO and PDO were in positive phases. The combined positive phases of the ENSO and PDO increased the positive SSTA in the eastern-central Equatorial Pacific, which increased the strength of the SPCZ and shifted it northeastward, thus decreasing the convergence over Fiji.

Figure 13c presents 130 Fiji wet events when the SPCZ was weak. The wettest events (54) took place when both the ENSO and PDO were in negative phases. The combined negative phases of the ENSO and PDO increased the negative SSTA in the eastern-central Equatorial Pacific, which decreased the strength of the SPCZ and shifted it southwestward, thus increasing the precipitation over Fiji.

Figure 13d presents 79 Fiji dry events when the SPCZ was weak. The combined positive phases of the ENSO and PDO mainly produced dry events (29).

Aggregating (a) and (c), and (b) and (d), we found that the combined positive phases of ENSO and PDO dominated the dry events while combined negative phases of ENSO and PDO dominated the wet events over Fiji. Here, we only distinguish the wet and dry events by positive and negative SPI. The purpose is to use as many samples as possible to demonstrate the general concept. In future studies, we will use more rigorous criteria to classify the wet and dry events.

Corresponding to the four categories in Figure 13, Figure 14 shows the composite outgoing longwave radiation (OLR) and low-level circulation at 850 mb derived from the ERA-Interim, and classified by strong and weak modes of the SPCZ and wet and dry conditions over Fiji. Figure 14a shows an anomalous convergence zone that laid from offshore Australia toward the southeast until 160 °W, which covered Fiji along its south boundary. The northeasterly anomaly brought warm, wet air from the tropics to Fiji. The anomalous convergence of warm, wet air produced extra rainfall over Fiji.

Figure 14b shows the circulation composite for dry events when the SPCZ was strong. The low-level circulation shows a cyclonic anomaly in the southeastern Equatorial Pacific, which weakened the eastern Pacific high, whereas the anticyclonic anomaly that lay offshore Australia enhanced the southeast trade winds in the western Pacific. Between the anomalous cyclone and anticyclone circulations, a broad anomalous divergence zone developed in the southern Pacific. The anomalous cold, dry air from the southeast passed Fiji and brought dry events. In the central Equatorial Pacific, the anomalous outflow from the divergence zone encountered the anomalous cross-equatorial flow from the Northern Hemisphere and generated a strong convergence anomaly, which might have enhanced the northeastward displacement of the SPCZ.

The circulation in Figure 14c is almost a reverse of the circulation in 14b. An anomalous cyclone offshore Australia weakened the trade winds while an anomalous high over the southeastern Equatorial Pacific enhanced the southeastern Pacific anticyclone. The combined effects of the anomalous low and high produced a strong convergence band oriented along a northwest/southeast axis over the southern Equatorial Pacific. This convergence band weakened the weak phase of the SPCZ and the wet air from the warm pool brought a large amount of rainfall to Fiji. Meanwhile, the central Equatorial Pacific experienced a strong divergent flow.

Figure 14d is the reverse of the circulation in Figure 14a. The general direction of flow was from southwest to east or northeast and there was a clear weak divergence area over Fiji. The local westerly winds embedded in the large-scale southwesterly winds brought cold, dry air to Fiji.

The situation in Figure 14b enhanced the strong SPCZ and corresponded to the positive phases of the ENSO and PDO in Figure 13b, while the anomaly in Figure 14c weakened the weak SPCZ and corresponded to the negative phases of the ENSO and PDO in Figure 13c. The overlapping positive phases of the ENSO and PDO strengthened the SPCZ northeastward and caused dry events in Fiji. The overlapping negative phases of the ENSO and PDO weakened the SPCZ southwestward and caused wet events in Fiji.

6.2 Production of 8 km WRF Model Outputs

6.2.1 Regional Simulation of Climatology over Fiji

Figure 15 compares the climatological low-level circulation of the ERA-Interim and the WRF_8km experiment, and their difference across four seasons. In the local summer season DJF (Figure 15a), the northeasterly originating from the southeastern Pacific high prevailed over Fiji and the adjacent ocean in the ERA-Interim. The warm, wet air came from the northeastern warm ocean. Figure 15e is the corresponding DJF simulation of the WRF_8km experiment. The geopotential height was slightly underestimated in the northwest region in WRF_8km. The northeasterly flow was adequately reproduced. The topographic effects were clearly visible over Viti Levu and Vanua Levu. Figure 15i shows the difference between the simulation and the ERA-Interim. In WRF_8km, the geopotential height was underestimated and the winds had northerly bias. However, the divergence over islands was clear. Convergence caused by the block effects of high topography and flow concentration behind lands was clearly generated by WRF_8km. This added value greatly impacted the model precipitation, while no such details were found in the low-resolution large-scale forcing fields.

Figure 15b shows the low-level circulation of the ERA-Interim in the local winter season JJA when the easterly trade winds prevailed in the region. WRF_8km adequately captured the easterlies in a high-resolution grid and showed a noticeable topographic effect over Viti Levu (Figure 15f). Their difference is shown in Figure 15j. Apart from the underestimation of geopotential height with corresponding northerly wind bias, the topographically added effect was seen clearly in the difference. The southwest/northeast orientation of Vanua Levu blocked the easterly and turned it southwestward. Viti Levu split the easterly and produced a southeasterly along its northern boundary. The effects of the topography generated an easterly convergence anomaly between the lands relative to the forcing field.

Figure 15c and 15g display the low-level circulation in the transient season MAM of the ERA-Interim and the WRF_8km, respectively. East-northeasterly winds prevailed in the region. WRF_8km adequately simulated the wind and geopotential height. Their difference (Figure 15k) generally shows the northerly wind and negative geopotential biases. The divergence and convergence anomalies caused by the topography were similar but weaker than those in DJF. Figure 15d, 15h, and 15l show the ERA-Interim, WRF_8km, and their difference in SON, respectively. East-northeasterly winds prevailed in SON. The WRF model adequately simulated geopotential height and wind direction. Similar bias as that in other seasons was found. The pattern of the convergence anomaly was as same as that in DJF, but with higher intensity in some areas.

Figure 16 displays the climatological rainfall comparison among CMORPH, the ERA-Interim, and WRF_8km in four seasons. Both CMORPH (Figure 16a) and WRF_8km (Figure 16i) show the heaviest rainfall in the rainy season DJF during the annual cycle, while the ERA-Interim rainfall (Figure 16e) in DJF was not very different from those in other seasons because the coarse resolution of reanalysis could not distinguish Viti Levu and Vanua Levu. JJA was the local winter dry season. CMORPH (Figure 16b) and WRF_8km (Figure 16j) captured the driest signals. WRF_8km also distinguished the relatively heavy rainfall on the windward side of Viti Levu and Vanua Levu. MAM was the local transient season following the summer. CMORPH (Figure 16c) poorly shows rainfall features caused by the topography over Viti Levu and Vanua Levu, while WRF_8km (Figure 16k) clearly shows the relatively heavy rainfall on the windward side of Viti Levu. WRF_8km (Figure 16l) also simulated the relatively heavy rainfall to the east and the light rainfall to the west of Viti Levu in SON. Generally, the ERA-Interim rainfall was highly correlated with satellite data from CMORPH. Most importantly, the WRF_8km model produced accurate rainfall measurements for all seasons.

6.2.2 Temporal Evolution of Rainfall

The red and blue lines in Figure 6 represent the monthly rainfall measured by WRF_8km and the ERA-Interim at the four weather stations. Rainfall measurements from both the WRF_8km and the ERA-Interim show a clear annual cycle. Although the rainfall of WRF_8km is slightly less correlated with the gauge rainfall, the rainfall measurement was more accurate than that from visual estimation as indicated by the root-mean-square error (RMSE) statistics.

Figure 7 compares the climatological annual rainfall cycle of WRF_8km, the ERA-Interim, and the gauge rainfall. Quantitatively, the WRF_8km annual cycle was very similar to the gauge annual cycle in terms of both correlation and RMSE, while rainfall from the ERA-Interim was far lower than the gauge throughout the cycle.

6.2.3 Spatial and Temporal Distribution of SPI

Figure 8 compares the observed SPI and simulated SPI in the WRF_8km experiment at the four weather stations. Their correlation coefficients were high. WRF_8km was capable of reproducing the successive 5-month dry events in 1983, 1987, and 1998.

Figure 17a shows the first EOF mode of the grid SPI in the WRF_8km experiment over land. The temporal variability of the wet and dry events was high at the central and eastern parts of Viti Levu and at southwestern parts of Vanua Levu. The eastern part Viti Levu and northeastern part of Vanua Levu have relatively uniform wet and dry anomalies temporally. On the other hand, all of the points had positive values, which means that the temporal variability of the SPI was in phase across all of the land grid points. Therefore, averaging SPIs of all of the land grid points would not cancel out the wet and dry events at the island scale. The averaged SPI (Figure 17b) reasonably presents the wet and dry alternatives over Viti Levu and Vanua Levu as shown in the comparison between Figure 17b and Figure 10b.

6.2.4 Composite Analysis of Simulated Wet and Dry Events

After we obtained the averaged SPI of WRF_8km, we were able to carry out the comparable composite study with WRF_8km circulation and wet and dry events. Figure 18 shows the composite of simulated OLR, u, and v at 850 mb classified by the simulated wet and dry conditions over Fiji and the strong and weak modes of the SPCZ from the ERA-Interim. Figure 18a shows a northwesterly anomaly converging with a northeasterly anomaly over Fiji. The warm, wet air from the tropics caused rainfall over Fiji. The negative anomalous OLR indicated convergence and anomalous rainfall over Fiji. Figure 18b shows the circulation composite for dry events when the SPCZ was strong. The strong anomalous divergence and the anomalous cold, dry air from the southwest passed Fiji and caused dry events. The circulation anomaly in Figure 18c was northwesterly and the convergence anomaly developed in the model domain. This convergence band weakened the weak phase of the SPCZ. The wet air anomaly from the warm pool brought anomalous rainfall to Fiji. Figure 18d shows that the anomalous southwesterly flowed toward the east and northeast. The cold, dry air from the southwest together with the divergence caused dry events in Fiji. Generally, the simulated weather patterns that caused the wet and dry events in the strong and weak SPCZ were very similar to the corresponding patterns in the composite study of the real observations. However, the model overestimated the dry (wet) event frequency when the SPCZ was strong (weak) and underestimated the dry (wet) event frequency when SPCZ was weak (strong).

Figure 19 shows the correlation between the SPCZ index and the model grid SPI derived from the rainfall in the WRF_8km simulation. Negative correlation coefficients less than -0.45 show that the SPCZ mainly influenced the SPI between the height of 200 m to 300 m over the leeward side, i.e., the dry side of the high mountain in Viti Levu, which agrees with the findings of Kumar et al. (2014). The areas less influenced were northeastern Viti Levu and the middle of Vanua Levu.

6.3 Bias Correction

Figure 6 compares the gauge rainfall and simulated rainfall in the WRF_8km simulation. Although the rainfall of WRF_8km was similar to the gauge data, biases still remained. To increase the reliability of using the model rainfall to predict future wet and dry events, bias correction was necessary. Numerous bias correction methods were invented in order to improve the quality of rainfall measurements from numerical models such as the additive method, quantile mapping method, rainfall frequency correction, and rainfall intensity correction (Ines and Hansen 2006; Piani et al. 2010). In this study we used the additive method for conditions of positive rainfall. There was a difference between observed rainfall and modeled rainfall at each weather station on the first day. We attempted to increase or decrease the modeled rainfall for the entire model domain in order to minimize the sum of the four absolute differences for conditions of positive adjusted rainfall in the domain. We then corrected the modeled rainfall every day of the experiment. This method optimized the temporal variability of the model rainfall and kept the spatial distribution untouched. The comparison between the original modeled rainfall and bias-corrected rainfall based on the gauge data is shown in Figure 20. The correction coefficients between the original modeled rainfall and gauge data were improved from 0.66, 0.66, 0.76, and 0.59 to 0.77, 0.82, 0.85, and 0.74 at Udu Point, Nabouwalu, Nadi, and Suva, respectively. The corresponding RMSEs decreased from 4.21, 4.21, 4.50, and 4.50 mm/d to 3.52, 3.02, 3.67, and 3.68 mm/d, respectively.

6.4 Development of a Drought Forecast Model

6.4.1 SPI6 Forecast Based on Bias-Corrected Climate Models (FCST_ONLY)

The performance of the SPI6 forecast calculated from bias-corrected climate models, including seven individual models such as the APCC MME (same as the input variable SPI6_FCST), was evaluated based on Drought Accuracy and MAE for drought categories (Figures 21 and 23). A 6-month period of accumulated rainfall was divided into two periods according to the lead-time of the forecast;

months with observed rainfall and months with forecasted rainfall. Remote sensing based precipitation data were used as the observed rainfall, and bias-corrected precipitation forecast data were used as the forecasted rainfall. Parameters for the gamma probability distribution functions were pre-fitted based on remote sensing based precipitation data and used for SPI6_FCST calculations.

When SPI6 obtained from in-situ precipitation data was used as reference data, Drought Accuracy for lead times of 1-2 months all had values of zero, and some models produced 0.17 Drought Accuracy for lead times of 3-6 months (Figure 21). These results were not expected because Drought Accuracy tends to decrease with increased lead-time. This may have happened because few drought events were assigned to the datasets for final evaluation due to the small number of samples. A scatter plot of observed vs. predicted SPI6 of MME with a 4-month lead-time is shown in Figure 22. Although total accuracy of drought categories was 0.68, Drought Accuracy was 0.17 in this case (Figure 21).

Due to the same reasons, the MAE of drought categories also did not show an increasing trend with lead-time. The APCC model produced the smallest MAE with a 1-month lead-time. The POAMA and MME models performed better with 2- to 5-month lead times, and the NCEP model showed the smallest MAE with a 6-month lead-time (Figure 23).

We also tested FCST_ONLY cases with reference data of SPI6_OBS from the WRF model outputs. In this case, decreasing Drought Accuracy and increasing MAE for drought categories were observed for all cases (Figures 24 and 25). Performance of climate models for the two performance measures was consistent; the PNU model performed the best with 1-month lead-time, and the NCEP model performed better with 2- to 3-month lead times. The POAMA model produced the highest Drought Accuracy and the lowest MAE with 4- to 6-month lead times (Figures 24 and 25). A scatter plot of observed vs. predicted SPI6 of PNU with a 1-month lead-time is shown in Figure 26.

6.4.2 SPI6 Forecast Based on Machine Learning Models

Hyper-parameters of machine learning models need to be optimized. The number of trees (among 10, 50, 100, and 200) and the maximum depth of tree growth (among 3, 5, and 10) were optimized for ERT, while the number of trees was optimized for Adaboost. Although trees may have been fully developed, up to 10 levels of depth were tested when reference data from the WRF model outputs were used due to the limitation of computational resources. MAE for drought categories was used as a primary performance measure for selecting hyper-parameters and the best climate model. Selected climate models, parameters, averaged Drought Accuracy, and MAE for drought categories from leave-one-out cross validation cases of training are given in Tables 2 and 3.

6.5 Validation of the Drought Forecast Model

Final evaluation was based on the three groups of datasets remaining using selected climate models. Drought Accuracy and MAE for drought categories for FCST_ONLY, ERT, and Adaboost were compared using the test datasets (Figures 27 to 30, Tables 4 and 5).

When reference data of SPI6_OBS from in-situ data were used, Drought Accuracy was zero except for 3-month lead forecasts (Figure 27). For MAE in drought categories, FCST_ONLY showed lower MAE than machine learning models except for 3-month lead forecasts (Figure 28).

The use of WRF model outputs for reference data of SPI6_OBS enhanced Drought Accuracy and reduced MAE for drought categories (Figures 29 and 30). FCST_ONLY performed well related to Drought Accuracy and MAE for drought categories with 1- and 2-month lead times, while ERT performed the best with 3- to 6-month lead times (Figures 29 and 30).

The performance of the methods and models used in this study needs to be compared with caution, because they could change with different performance measures. In this study, MAE for drought categories was used as a primary performance measure. Hyper-parameters of machine learning models and best climate models were selected based on the MAE values. Other measures including Total Accuracy for all SPI categories, Drought Accuracy, MAE for all SPI categories, correlation coefficient (r) for all SPI categories, and correlation coefficient (r) for drought categories may also be used. For example, the performance of FCST_ONLY with NCEP was the highest among methods for 2-month lead times based on reference data of SPI6_OBS from the WRF model outputs, and the MAE was 0.69. The MAE of ERT with PNU was 0.74, which is higher than the previous mentioned case. When the correlation coefficient (r) values for drought categories were compared, the (r) value of ERT was higher (r = 0.35; Figure 31) than FCST_ONLY (r = 0.22; Figure 32).

Spatial distribution maps of drought forecasts for Fiji based on ERT were created and compared to remote sensing based SPI values (e.g., Figure 33).

7. CONCLUSION

A drought forecast model for Fiji was developed based on high-resolution dynamic downscaling of climate data and machine learning of long-range climate forecast and remote sensing data.

The WRF_8km experiment adequately simulated the low-level circulation and rainfall distribution, providing accurate rainfall amounts for all seasons, although the geopotential height was slightly underestimated and the winds contained a small northerly bias. However, the added value caused by the topography was clear, especially in the convergence/divergence field over the islands. This crucially impacted inland and coastal precipitation and caused greater detail in precipitation to be found in the WRF_8km output.

The SPI derived from the rainfall time series was used to measure the wet and dry events for both gauge observation and downscaling results. All SPIs from gauge data and from model rainfall showed consistent temporal variability over space. Apart from the historical severe dry seasons, a clear dry trend could not be found from the SPIs in the recent 30 years from 1981 to 2010. WRF_8km results showed that the leeward area between 200 m to 300 m in elevation was very sensitive to the SPCZ variability.

Composite analysis of observed data confirmed that the strong SPCZ tended to cause dry events and weak SPCZ tended to cause wet events over Fiji. The combined positive (negative) phases of the ENSO and PDO had a high probability of producing dry (wet) events over Fiji. When ENSO and PDO were out of phase, the large-scale system did not usually generate wet or dry events, with the existence of one exception. When ENSO and PDO were in positive (negative) phases, the SPCZ was weak (strong) and wet (dry) events happened over Fiji. When the SPCZ was strong (weak), low-level circulation anomalies weakened (enhanced) the eastern Pacific high but enhanced (weakened) the southeast trade winds in the western Pacific. This developed an anomalous divergence (convergence) band that covered Fiji in the southern Pacific with anomalous outflow (inflow) converging (diverging) at (from) the central Equatorial Pacific, resulting in dry (wet) events over Fiji. Wet (dry) events also took place when the SPCZ was strong (weak); however, the frequency and intensity of the events were much lower and weaker, respectively.

The composite study of the WRF_8km output provided results very similar to those from the observations, which indicated reasonable responses of the downscaled wet and dry events to the anomalous large-scale patterns. This promised a solid ground on which the drought prediction model could be built. Furthermore, bias-corrected rainfall, which outperformed the raw model rainfall, was used in the drought forecast model to further increase reliability.

Drought index SPI6 was used as a target variable indicating drought conditions. Machine learning models were trained using the drought index calculated using in-situ data. There are few weather stations with available precipitation data, which resulted in insufficient datasets for training of machine learning models. Limited distribution of weather stations may also hamper examination of spatial characteristics of drought occurrences.

Bias-corrected WRF model precipitation outputs with 8 km spatial resolution were used to calculate SPI6_OBS instead of the index using in-situ data. The use of these WRF model outputs mostly increased Drought Accuracy and decreased MAE for drought categories in SPI6 forecasting, especially those with shorter lead times, whether bias-corrected climate model outputs or machine learning models were used.

Machine learning models provide information of relative importance about input variables. Relative importance of remote sensing variables was relatively low compared to large-scale climate indices such as MEI and SPCZ strength (data not shown). Since remote sensing variables limit the length of datasets of machine learning models, longer datasets using only the input variables with available data for the period will be tested in a further study.

It should be noted that the performance of the machine learning models and climate models used in this study were only partially analyzed for the purpose of this specific study. As previously mentioned, the performance of the compared methods can be evaluated differently according to the choice of performance measure.

A brief guideline on use of the drought forecast model developed in this study is presented in Appendix A.

APPENDIX A

Appendix A. Guideline for the Application of the Drought Forecast Model

Based on the results of the experiments of this study, we have put together brief suggestions on the procedures used to apply a drought forecast model. The suggested procedures to forecast SPI6 below are written based on the assumption that an operational system for the models tested in this study is already developed, including the development of a database with historical input data that is updated regularly. Detailed guidelines and examples will be developed in the following year for a training and technical workshop in Fiji.

A.1 Select a Drought Index

Users can select the time scale of SPI; 1-, 3-, 6-, 9-, 12-, and 24-month time scales are shown in the report of WMO recommending the use of SPI (Hayes et al. 2011). SPI6 was used in this study.

A.2 Select Performance Measures

As mentioned in the main text, various performance measures are available including Total Accuracy, MAE, and correlation coefficient (r) for all SPI categories as well as drought categories (Moderate Drought, Severe Drought, and Extreme Drought). In this study, Drought Accuracy and MAE for drought categories were examined for compared cases, but the MAE for drought categories was used as a primary performance measure for selecting hyper-parameters and the best climate models.

A.3 Select a Method and Climate Model

A method (one of the machine learning models of ERT and Adaboost or FCST_ONLY) and the best climate model for the method can be selected based on the performance measure chosen. Sometimes more than one performance measure may be utilized; some user decisions are involved in this process. Based on the results of this study, the users may select the FCST_ONLY method with the selected climate models for each lead-time. If the user also wants to consider the correlation coefficient values for drought categories together, a machine learning model, ERT, may be chosen.

A.4 Create Spatially Distributed SPI6 Forecast Maps

The programming codes are written in Python. Using the database with spatially distributed GeoTiff data for Fiji and the files of pre-built models, spatially distributed SPI6 forecast maps can be created. The maps enable the users to examine the spatial characteristics of future drought occurrences.

A.5 Create Zonal Average Maps

Drought forecast information could be more useful when given for each administrative unit or watershed basin unit. Using Geographic Information Systems, zonal averages can be derived for desired spatial units. Commercial packages, such as ArcGIS, as well as open-source software, such as QGIS, can be used for such tasks.

Acknowledgements

We would like to thank two reviewers for their insightful and constructive suggestions.

REFERENCES

AghaKouchak A., Behrangi A., Sorooshian S., Hsu K., Amitai E. (2011) Evaluation of satellite-retrieved extreme precipitation rates across the central United States. J Geophys Research: Atmospheres

Agrawala S., Ota T., Risbey J., Hagenstad M., Smith J., van Aalst M., Koshy K., Prasad B. (2003) Development and Climate Change in Fiji: Focus on coastal mangroves. OECD

Arakawa A. (2004) The cumulus parameterization problem: Past, present, and future. J Clim 17:2493–2525

Ashouri H., Hsu K.-L., Sorooshian S., Braithwaite D.K., Knapp K.R., Cecil L.D., Nelson B.R., Prat O.P. (2015) PERSIANN-CDR: Daily precipitation climate data record from multisatellite observations for hydrological and climate studies. Bull Am Meteorol Soc 96:69–83

Beljaars A. (1995) The parametrization of surface fluxes in large-scale models under free convection. Q J R Meteorol Soc 121:255–270

Bergeron T. (1930) Richtlinien einer dynamischen Klimatologie. Meteorologische Zeitschrift 47:246–262

Borlace S., Santoso A., Cai W., Collins M. (2014) Extreme swings of the South Pacific Convergence Zone and the different types of El Niño events. Geophys Res Lett 41:4695–4703

Cai W., Lengaigne M., Borlace S., Collins M., Cowan T., McPhaden M.J., Timmermann A., Power S., Brown J., Menkes C., others (2012) More extreme swings of the South Pacific convergence zone due to greenhouse warming. Nature 488:365–369

Chattopadhyay M., Katzfey J. (2015) Simulating the climate of South Pacific islands using a high resolution model. Int J Climatol 35:1157–1171

Collins W.D., Rasch P.J., Boville B.A., Hack J.J., McCaa J.R., Williamson D.L., Kiehl J.T., Briegleb B., Bitz C., Lin S.J., others (2004) Description of the NCAR community atmosphere model (CAM 3.0). Ncar Tech. Note Ncar/Tn-464+ Str

Davies H.C., Turner R_E. (1977) Updating prediction models by dynamical relaxation: An examination of the technique. Q J R Meteorol Soc 103:225–245

Dee D.P., Uppala S.M., Simmons A.J., Berrisford P., Poli P., Kobayashi S., Andrae U., Balmaseda M.A., Balsamo G., Bauer P., others (2011) The ERA-Interim reanalysis: Configuration and performance of the data assimilation system. Q J R Meteorol Soc

137:553–597

Deo R.C. (2011) On meteorological droughts in tropical Pacific Islands: time-series analysis of observed rainfall using Fiji as a case study. Meteorol Appl 18:171–180

Derrick R.A. (1957) The Fiji Islands: a geographical handbook. Government Press

Dyer A.J., Hicks B.B. (1970) Flux-gradient relationships in the constant flux layer. Q J R Meteorol Soc 96:715–721

Feresi J., Kenny G.J., de Wet N., Limalevu L., Bhusan J., Ratukalou I. (2000) Climate change vulnerability and adaptation assessment for Fiji. Technical Report, The International Global Change Institute (IGCI), University of Waikato.

Folland C.K., Renwick J.A., Salinger M.J., Mullan A.B. (2002) Relative influences of the interdecadal Pacific oscillation and ENSO on the South Pacific convergence zone. Geophys Res Lett

Gerard L. (2007) An integrated package for subgrid convection, clouds and precipitation compatible with meso-gamma scales. Q J R Meteorol Soc 133:711–730

Guttman N.B. (1999) Accepting the standardized precipitation index: a calculation algorithm. Jawra J Am Water Resources Association 35:311–322

Han P., Wang P.X., Zhang S.Y., Zhu D.H. (2010) Drought forecasting based on the remote sensing data using ARIMA models. Mathematical Computer Model 51:1398–1403

Hay J.E., Mimura N., Campbell J., Fifita S., Koshy K., McLean R.F., Nakalevu T., Nunn P., Wet N.d. (2003) Climate variability and change and sea-level rise in the Pacific Islands region: a resource book for policy and decision makers, educators and other stakeholders. SPREP Tokio, Japan

Hayes M., Svoboda M., Wall N., Widhalm M. (2011) The Lincoln declaration on drought indices: universal meteorological drought index recommended. Bull Am Meteorol Soc 92:485–488

Hong S.-Y., Dudhia J., Chen S.-H. (2004) A revised approach to ice microphysical processes for the bulk parameterization of clouds and precipitation. Mon Weather Rev 132:103–120

Hong S.-Y., Noh Y., Dudhia J. (2006) A new vertical diffusion package with an explicit treatment of entrainment processes. Mon Weather Rev 134:2318–2341

Hu Z.-Z., Huang B. (2009) Interferential impact of ENSO and PDO on dry and wet conditions in the US Great Plains. J Clim 22:6047–6065

Huang B., Banzon V.F., Freeman E., Lawrimore J., Liu W., Peterson T.C., Smith T.M., Thorne

P.W., Woodruff S.D., Zhang H.-M. (2015) Extended reconstructed sea surface temperature version 4 (ERSST. v4). Part I: upgrades and intercomparisons. J Clim 28:911-930

Iacono M.J., Delamere J.S., Mlawer E.J., Shephard M.W., Clough S.A., Collins W.D. (2008) Radiative forcing by long-lived greenhouse gases: Calculations with the AER radiative transfer models. J Geophys Research: Atmospheres

Ines A.V., Hansen J.W. (2006) Bias correction of daily GCM rainfall for crop simulation studies. Agric For Meteorol 138:44-53

Jensen J.R., Lulla K. (1987) Introductory digital image processing: a remote sensing perspective. Taylor \& Francis

Joyce R.J., Janowiak J.E., Arkin P.A., Xie P. (2004) CMORPH: A method that produces global precipitation estimates from passive microwave and infrared data at high spatial and temporal resolution. J Hydrometeorol 5:487-503

Jung T., Miller M.J., Palmer T.N., Towers P., Wedi N., Achuthavarier D., Adams J.M., Altshuler E.L., Cash B.A., Kinter Iii J.L., others (2012) High-resolution global climate simulations with the ECMWF model in Project Athena: Experimental design, model climate, and seasonal forecast skill. J Clim 25:3155-3172

Kain J.S. (2004) The Kain-Fritsch convective parameterization: an update. J Appl Meteorol 43:170-181

Kain J.S., Fritsch J.M. (1990) A one-dimensional entraining/detraining plume model and its application in convective parameterization. J Atmos Sci 47:2784-2802

Kidwell A., Lee T., Jo Y.-H., Yan X.-H. (2016) Characterization of the variability of the South Pacific convergence zone using satellite and reanalysis wind products. J Clim 29:1717-1732

Klemp J.B., Wilhelmson R.B. (1978) The simulation of three-dimensional convective storm dynamics. J Atmos Sci 35:1070-1096

Kumar R., Stephens M., Weir T. (2013) Temperature trends in Fiji: a clear signal of climate change. South Pacific J Natural Appl Sci 31:27-38

Kumar R., Stephens M., Weir T. (2014) Rainfall trends in Fiji. Int J Climatol 34:1501-1510

Lal M., McGregor J.L., Nguyen K.C. (2008) Very high-resolution climate simulation over Fiji using a global variable-resolution model. Clim Dyn 30:293-305

Laprise R. (1992) The Euler equations of motion with hydrostatic pressure as an independent variable. Mon Weather Rev 120:197-207

Leilah A.A., Al-Khateeb S.A. (2005) Statistical analysis of wheat yield under drought conditions. J Arid Environments 61:483-496

Liu H.Q., Huete A. (1995) A feedback based modification of the NDVI to minimize canopy background and atmospheric noise. Ieee Trans On Geosci Remote Sens 33:457-465

Mantua N.J., Hare S.R. (2002) The Pacific decadal oscillation. J Oceanogr 58:35-44

Mantua N.J., Hare S.R., Zhang Y., Wallace J.M., Francis R.C. (1997) A Pacific interdecadal climate oscillation with impacts on salmon production. Bull Am Meteorol Soc 78:1069-1079

Mataki M., Koshy K.C., Lal M. (2006) Baseline climatology of Viti Levu (Fiji) and current climatic trends. Pacific Sci 60:49-68

McKee T.B., Doesken N.J., Kleist J., others (1993) The relationship of drought frequency and duration to time scales. Proceedings of the 8th Conference on Applied Climatology 17:179-183

Mishra A.K., Singh V.P. (2011) Drought modeling-A review. J Hydrology 403:157-175

Morid S., Smakhtin V., Bagherzadeh K. (2007) Drought forecasting using artificial neural networks and time series of drought indices. Int J Climatol 27:2103-2111

Nicholls N., Wong K.K. (1990) Dependence of rainfall variability on mean rainfall, latitude, and the Southern Oscillation. J Clim 3:163-170

Ooyama K.V. (1990) A thermodynamic foundation for modeling the moist atmosphere. J Atmos Sci 47:2580-2593

Paulson C.A. (1970) The mathematical representation of wind speed and temperature profiles in the unstable atmospheric surface layer. J Appl Meteorol 9:857-861

Piani C., Haerter J.O., Coppola E. (2010) Statistical bias correction for daily precipitation in regional climate models over Europe. Theor Appl Climatol 99:187-192

Quan X.-W., Hoerling M.P., Lyon B., Kumar A., Bell M.A., Tippett M.K., Wang H. (2012) Prospects for dynamical prediction of meteorological drought. J Appl Meteorol Climatol 51:1238-1252

Rhee J., Im J. (2017) Meteorological drought forecasting for ungauged areas based on machine learning: Using long-range climate forecast and remote sensing data. Agric For Meteorol 237:105-122

Rhee J., Im J., Carbone G.J. (2010) Monitoring agricultural drought for arid and humid regions using multi-sensor remote sensing data. Remote Sens Environ 114:2875-2887

Risbey J.S., Lamb P.J., Miller R.L., Morgan M.C., Roe G.H. (2002) Exploring the structure of regional climate scenarios by combining synoptic and dynamic guidance and GCM output. J Clim 15:1036–1050

Rummukainen M. (2010) State-of-the-art with Regional Climate Models. Wiley Interdisciplinary Reviews: Clim Chang 1:82–96

Skamarock W.C., Klemp J.B. (1992) The stability of time-split numerical methods for the hydrostatic and the nonhydrostatic elastic equations. Mon Weather Rev 120:2109–2127

Skamarock W.C., Klemp J.B., Dudhia J., Gill D.O., Barker D.M., Wang W., Powers J.G. (2005) A description of the advanced research WRF version 2. Technical Report, National Center For Atmospheric Research Boulder Co Mesoscale and Microscale Meteorology Div

Solomon S. (2007) Climate change 2007-the physical science basis: Working group I contribution to the fourth assessment report of the IPCC. Cambridge University Press

Steinemann A.C. (2006) Using climate forecasts for drought management. J Appl Meteorol Climatol 45:1353–1361

Stocker T. (2014) Climate change 2013: the physical science basis: Working Group I contribution to the Fifth assessment report of the Intergovernmental Panel on Climate Change. Cambridge University Press

Tadesse T., Brown J.F., Hayes M.J. (2005) A new approach for predicting drought-related vegetation stress: Integrating satellite, climate, and biophysical data over the US central plains. Isprs J Photogrammetry Remote Sens 59:244–253

Terry J.P., Raj R. (1999) The 1997–98 El Niño and drought in the Fiji Islands. Hydrology and water management in the humid tropics. Proceedings of the second international colloquium pages 22–26

Terry J.P., Raj R. (1998) Hydrological drought in western Fiji and the contribution of tropical cyclones. Clim Environ Chang Pacific

Tewari M., Chen F., Wang W., Dudhia J., LeMone M.A., Mitchell K., Ek M., Gayno G., Wegiel J., Cuenca R.H. (2004) Implementation and verification of the unified NOAH land surface model in the WRF model. 20th conference on weather analysis and forecasting/16th conference on numerical weather prediction

Thompson G., Field P.R., Rasmussen R.M., Hall W.D. (2008) Explicit forecasts of winter precipitation using an improved bulk microphysics scheme. Part II: Implementation of a new snow parameterization. Mon Weather Rev 136:5095–5115

Trenberth K.E. (1976) Spatial and temporal variations of the Southern Oscillation. Q J R Meteorol Soc 102:639–653

Trenberth K.E., Hoar T.J. (1996) The 1990-1995 El Niño-Southern Oscillation event: Longest on record. Geophys Res Lett 23:57-60

Tucker C.J. (1979) Red and photographic infrared linear combinations for monitoring vegetation. Remote Sens Environ 8:127-150

Vincent E.M., Lengaigne M., Menkes C.E., Jourdain N.C., Marchesiello P., Madec G. (2011) Interannual variability of the South Pacific Convergence Zone and implications for tropical cyclone genesis. Clim Dyn 36:1881-1896

Wang S., Sobel A.H., Zhang F., Sun Y.Q., Yue Y., Zhou L. (2015) Regional simulation of the October and November MJO events observed during the CINDY/DYNAMO field campaign at gray zone resolution. J Clim 28:2097-2119

Webb E.K. (1970) Profile relationships: The log-linear range, and extension to strong stability. Q J R Meteorol Soc 96:67-90

Wicker L.J., Skamarock W.C. (2002) Time-splitting methods for elastic models using forward time schemes. Mon Weather Rev 130:2088-2097

Yang H.-W. (2013) Revision of climate change by dynamic downscaling over the maritime continents. Technical Report, APEC Climate Center

Yang H.-W. (2015) Dynamic downscaling of climate change over the maritime continents. Technical Report, APEC Climate Center

Yin H., Donat M.G., Alexander L.V., Sun Y. (2015) Multi-dataset comparison of gridded observed temperature and precipitation extremes over China. Int J Climatol 35:2809-2827

Yu X., LEE T.-Y. (2010) Role of convective parameterization in simulations of a convection band at grey-zone resolutions. Tellus A 62:617-632

Zhang D., Anthes R.A. (1982) A high-resolution model of the planetary boundary layer-Sensitivity tests and comparisons with SESAME-79 data. J Appl Meteorol 21:1594-1609

TABLES

Table 1. Fiji rainfall gauges used in the analysis.

Observation Sites	Latitude	Longitude
Udu Point	16.133 °S	180.017 °E
Nabouwalu	17 °S	178.7 °E
Nadi	17.755 °S	177.443 °E
Suva	18.15 °S	178.45 °E

Table 2. Selection of hyper-parameters and best climate models for each lead time and machine learning model, with reference data of SPI6_OBS from in-situ data.

Climate Model	Lead Time	Machine Learning Model	Number of Trees	Maximum Depth of Growth	Drought Accuracy	MAE for Drought Categories	Correlation Coefficient
PNU	1	Adaboost	50		0.3	0.75	-0.01
POAMA	2		10		0.16	0.86	0.04
POAMA	3		10		0.21	0.99	-0.11
POAMA	4		10		0.02	1.24	0.13
POAMA	5		10		0.0	1.29	0.05
CMCC	6		10		0.0	1.41	-0.04
PNU	1	ERT	200	3	0.28	0.66	0.1
PNU	2		200	3	0.15	0.82	0.1
POAMA	3		10	5	0.12	0.97	0.01
POAMA	4		10	5	0.01	1.17	0.16
PNU	5		10	3	0.0	1.35	0.16
NCEP	6		10	None	0.03	1.31	0.21

Table 3. Selection of hyper-parameters and best climate models for each lead time and machine learning model, with reference data of SPI6_OBS from the WRF model outputs.

Climate Model	Lead Time	Machine Learning Model	Number of Trees	Maximum Depth of Growth	Drought Accuracy	MAE for Drought Categories	Correlation Coefficient
PNU	1	Adaboost	10		0.05	1.14	0.25
POAMA	2		10		0.0	1.26	0.24
POAMA	3		50		0.02	1.31	0.31
POAMA	4		10		0.0	1.31	0.2
POAMA	5		10		0.05	1.32	0.24
CMCC	6		10		0.02	1.34	0.21
PNU	1	ERT	10	10	0.12	0.9	0.37
PNU	2		10	10	0.06	1.05	0.34
POAMA	3		200	10	0.07	1.05	0.34
POAMA	4		10	10	0.08	1.06	0.31
PNU	5		10	10	0.06	1.08	0.33
NCEP	6		10	10	0.06	1.09	0.33

Table 4. Drought Accuracy and MAE of drought categories for each lead time. Forecast methods of ERT, Adaboost, and FCST_ONLY with selected climate models, based on reference data of SPI6_OBS from in-situ data.

Measure	LT (month)		ERT	Adaboost		FCST ONLY	
MAE	1	1.2	PNU	1.12	PNU	1.05	APCC
	2	1.24	PNU	1.39	POAMA	1.07	POAMA
	3	1.06	POAMA	1.23	POAMA	1.08	POAMA
	4	1.67	POAMA	1.51	POAMA	1.09	POAMA, MME
	5	1.3	PNU	1.22	POAMA	1.06	MME
	6	1.48	NCEP	1.4	CMCC	0.96	NCEP
Drought Accuracy	1	0	PNU	0	PNU	0	
	2	0	CMCC	0	POAMA	0	
	3	0.17	POAMA	0.17	POAMA	0.17	NCEP, POAMA
	4	0	CMCC	0	MME	0.17	APCC, NASA, MME
	5	0	POAMA	0	MME	0.17	APCC, MME
	6	0	APCC	0	MSC	0.17	CMCC, NCEP, MME

Table 5. Drought Accuracy and MAE of drought categories for each lead time. Forecast methods of ERT, Adaboost, and FCST_ONLY with selected climate models, based on reference data of SPI6_OBS from the WRF model outputs.

Measure	LT (month)		ERT	Adaboost		FCST ONLY	
MAE	1	0.67	PNU	0.77	PNU	0.59	PNU
	2	0.74	PNU	0.79	POAMA	0.69	NCEP
	3	0.77	POAMA	0.92	POAMA	0.84	NCEP
	4	0.68	POAMA	1.01	NCEP	1.01	POAMA
	5	0.76	POAMA	1.02	APCC	1.22	POAMA
	6	0.8	POAMA	1.02	APCC	1.41	POAMA
Drought Accuracy	1	0.15	CMCC	0.21	MME	0.32	PNU
	2	0.12	MME	0	NCEP	0.2	NCEP
	3	0.14	POAMA	0.04	MME	0.11	NCEP
	4	0.18	POAMA	0.01	MSC	0.08	POAMA
	5	0.12	POAMA	0.01	APCC	0.05	POAMA
	6	0.1	POAMA	0	MME	0.03	POAMA

FIGURES

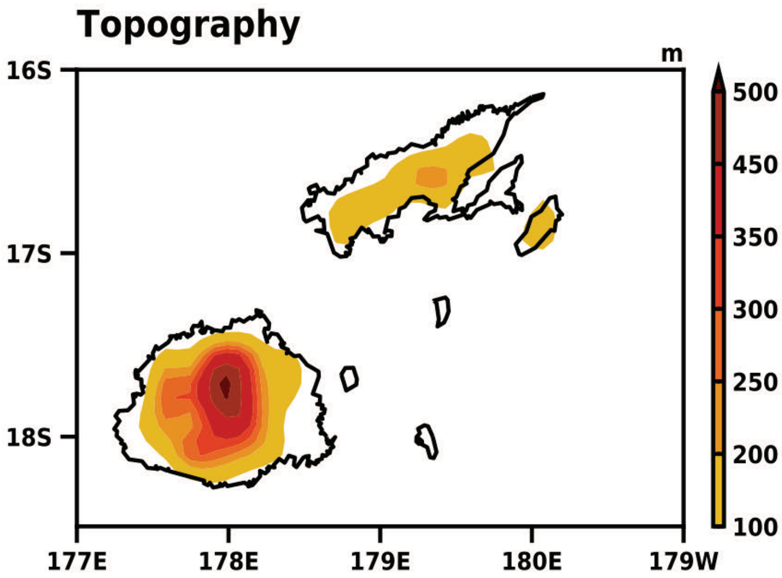

Figure 1. Topography of Fiji main islands (color shades are in units of meters).

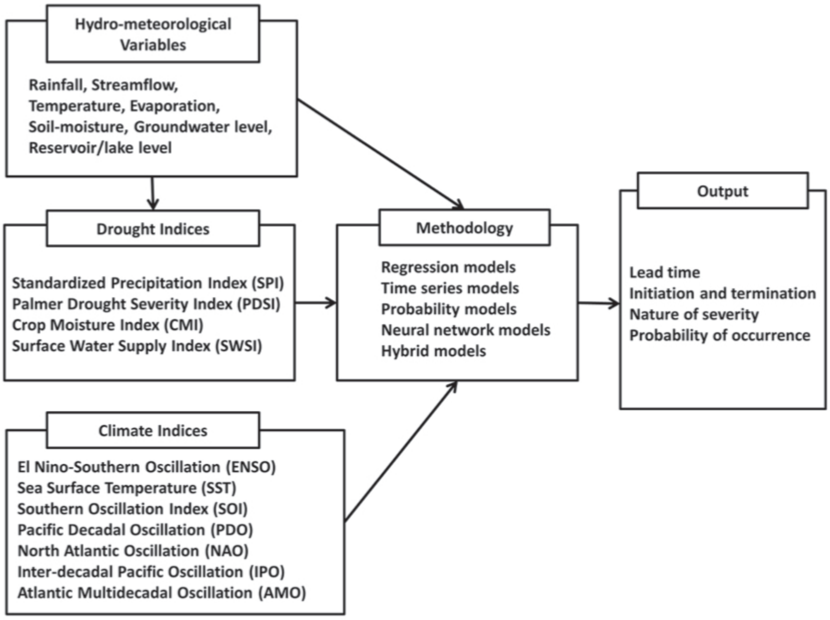

Figure 2. Components for drought forecasting (adapted from Mishra and Singh 2011).

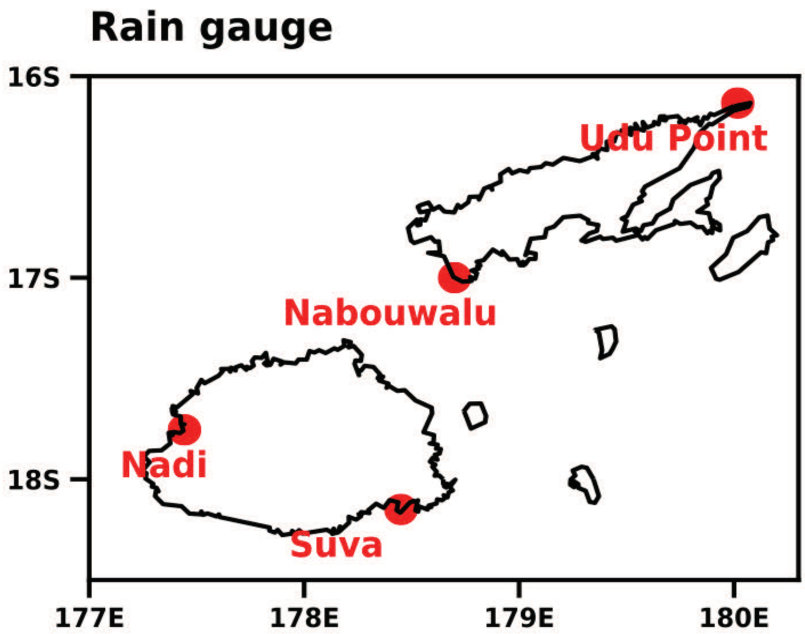

Figure 3. Location of rainfall gauges used in this report.

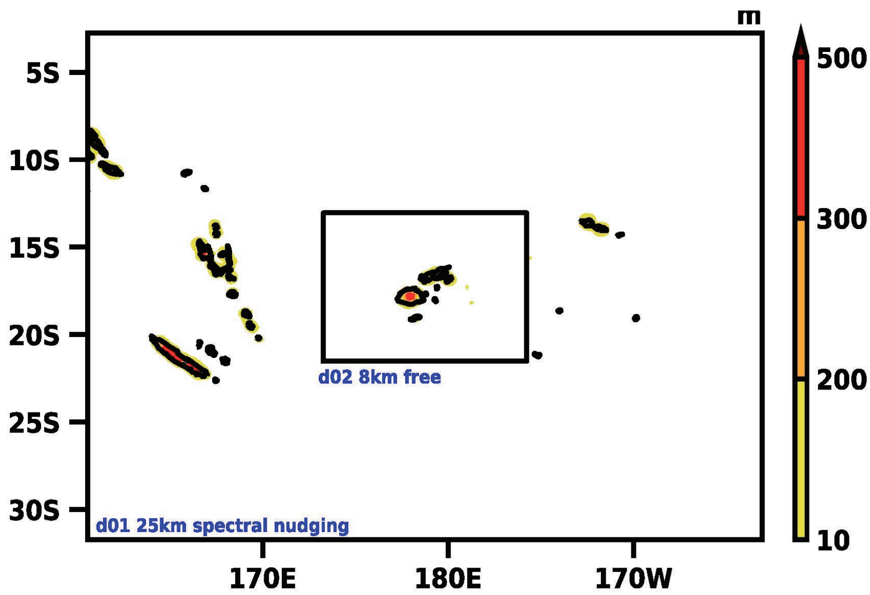

Figure 4. Model domain. Mother domain (31.5–2.8 °S, 160–197 °E) with 25 km horizontal resolution, nested domain (21–13 °S, 173–184 °E) with 8 km resolution, and topography (color shades are in units of meters).

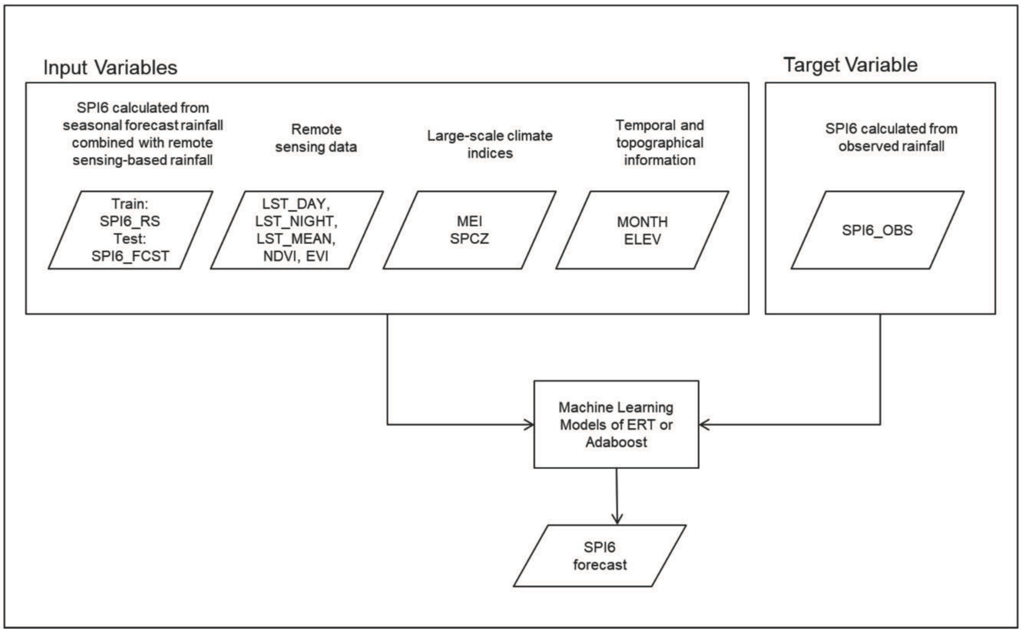

Figure 5. Flow diagram of the drought forecast model.

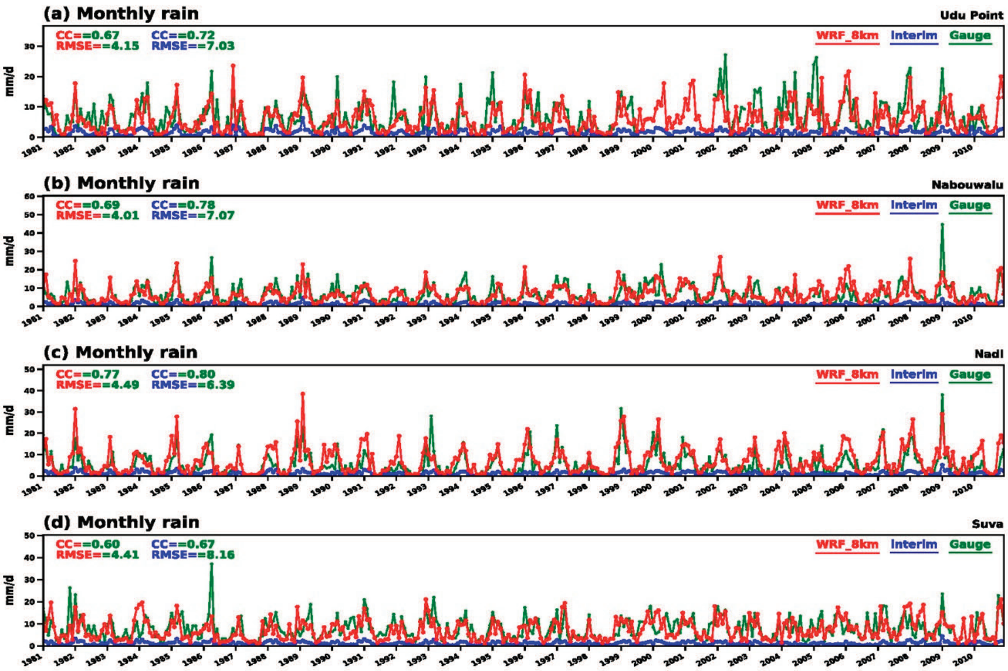

Figure 6. Monthly rainfall time series observations, the ERA-Interim data, and WRF_8km simulation at the gauge locations.

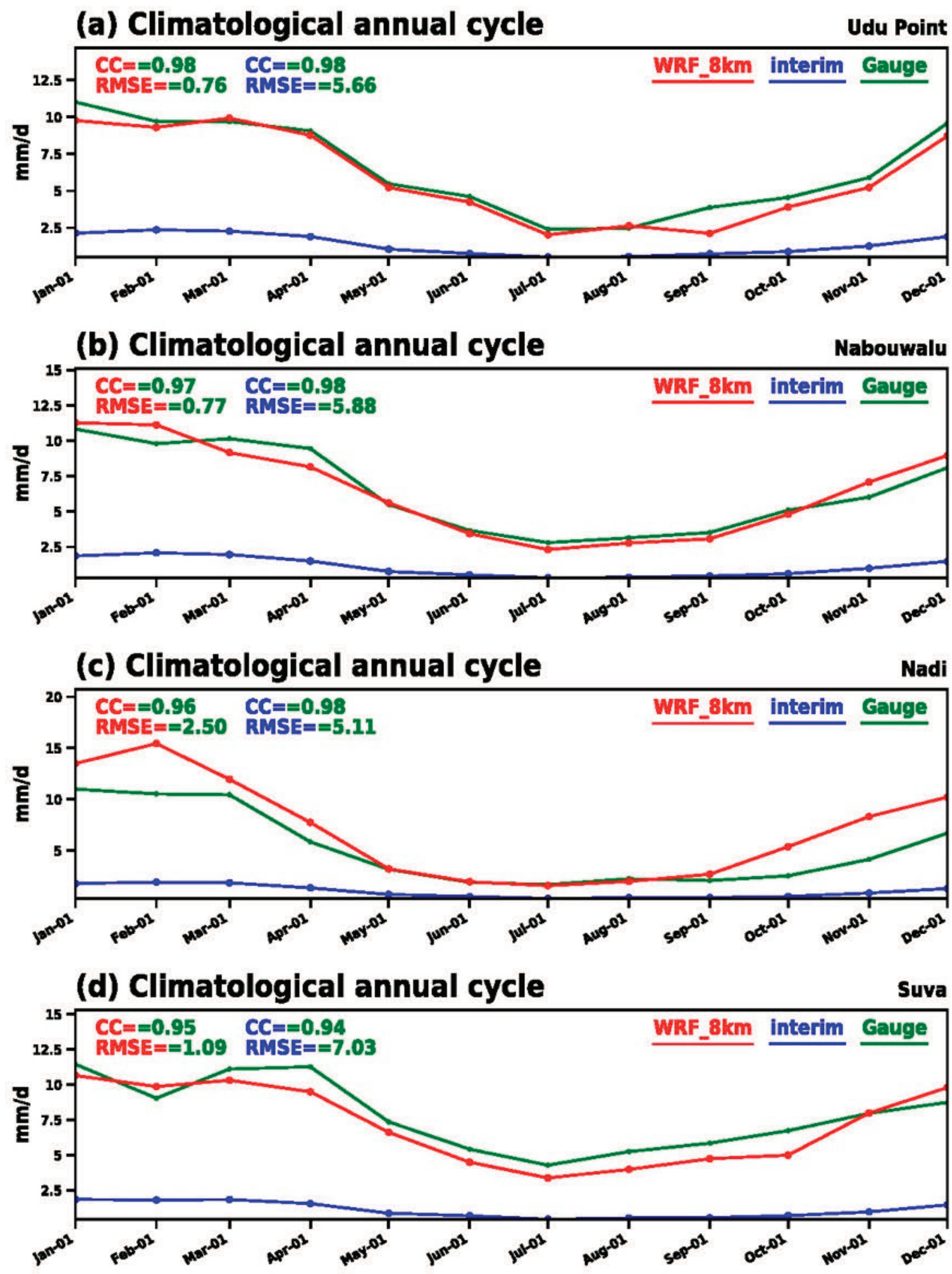

Figure 7. Climatological annual cycle observations, the ERA-Interim data, and WRF_8km simulation at the gauge locations.

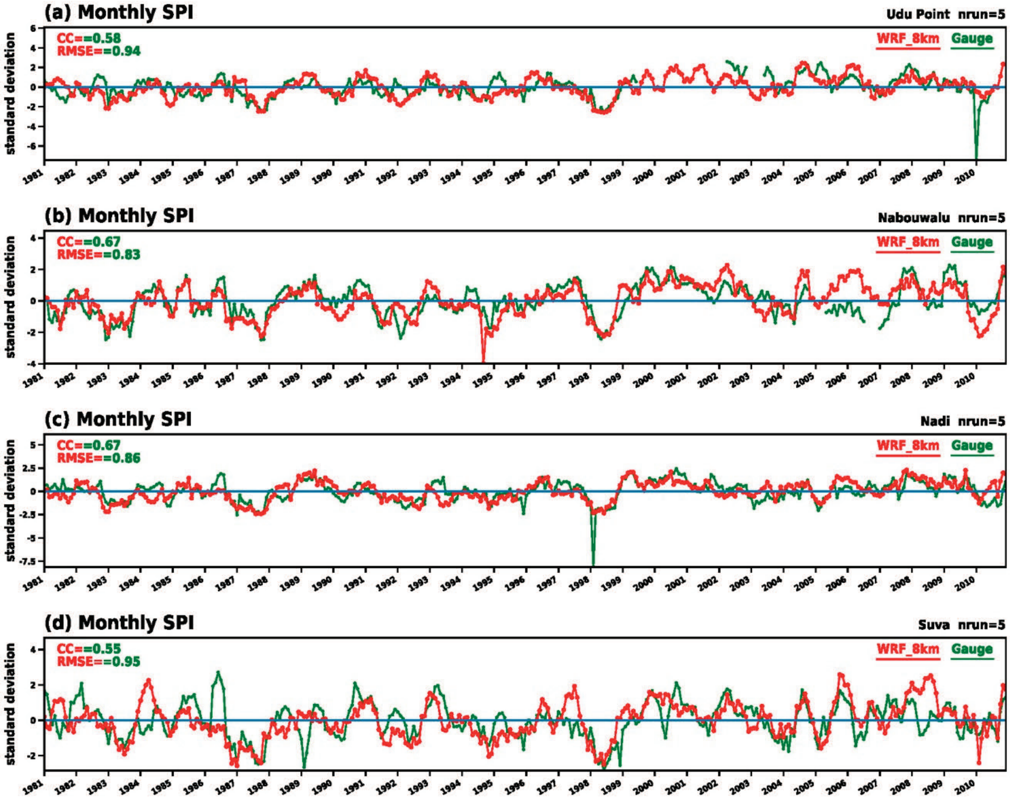

Figure 8. Five-month SPI observations and WRF_8km simulation at the gauge locations.

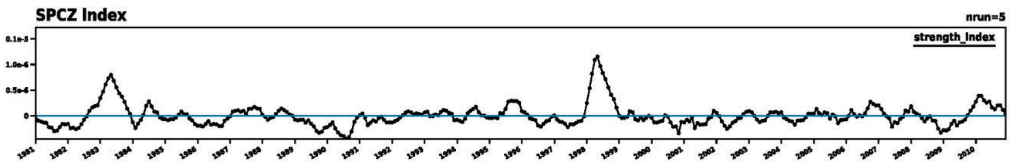

Figure 9. Five-month running mean of SPCZ strength index calculated from the ERA-Interim.

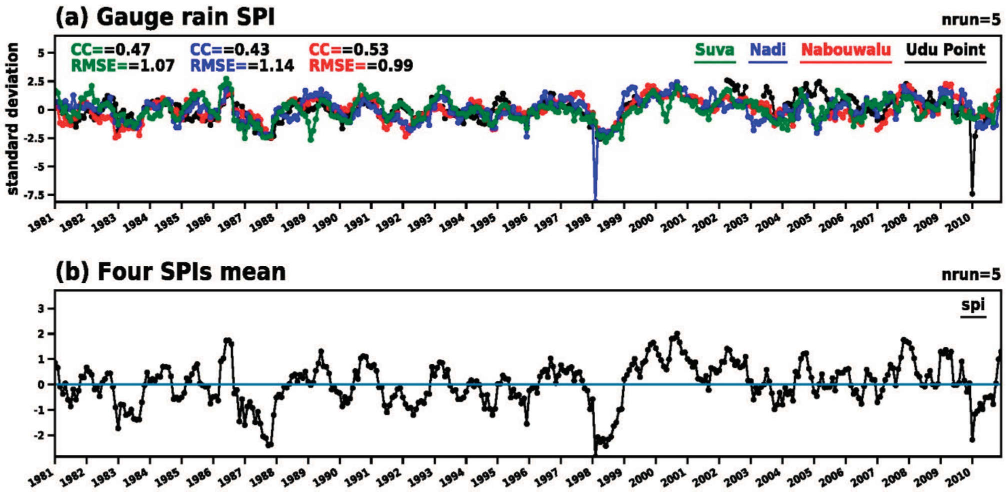

Figure 10. Correlation among 5-month SPIs and the mean of the SPIs at four gauges.

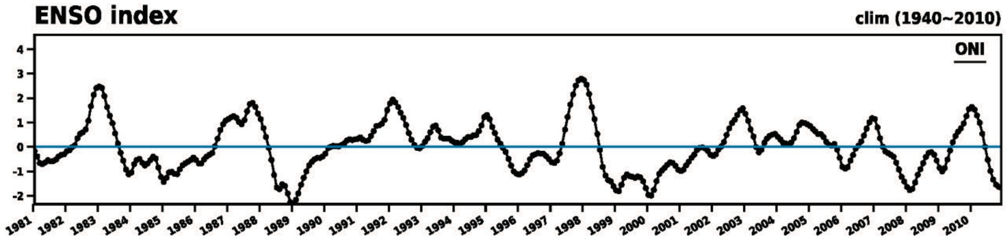

Figure 11. ONI derived from the ERSST based on the climatology from 1940 to 2010.

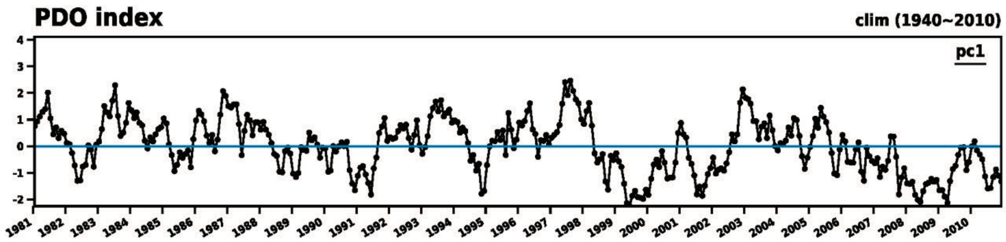

Figure 12. PDO index derived from the ERSST based on the climatology from 1940 to 2010.

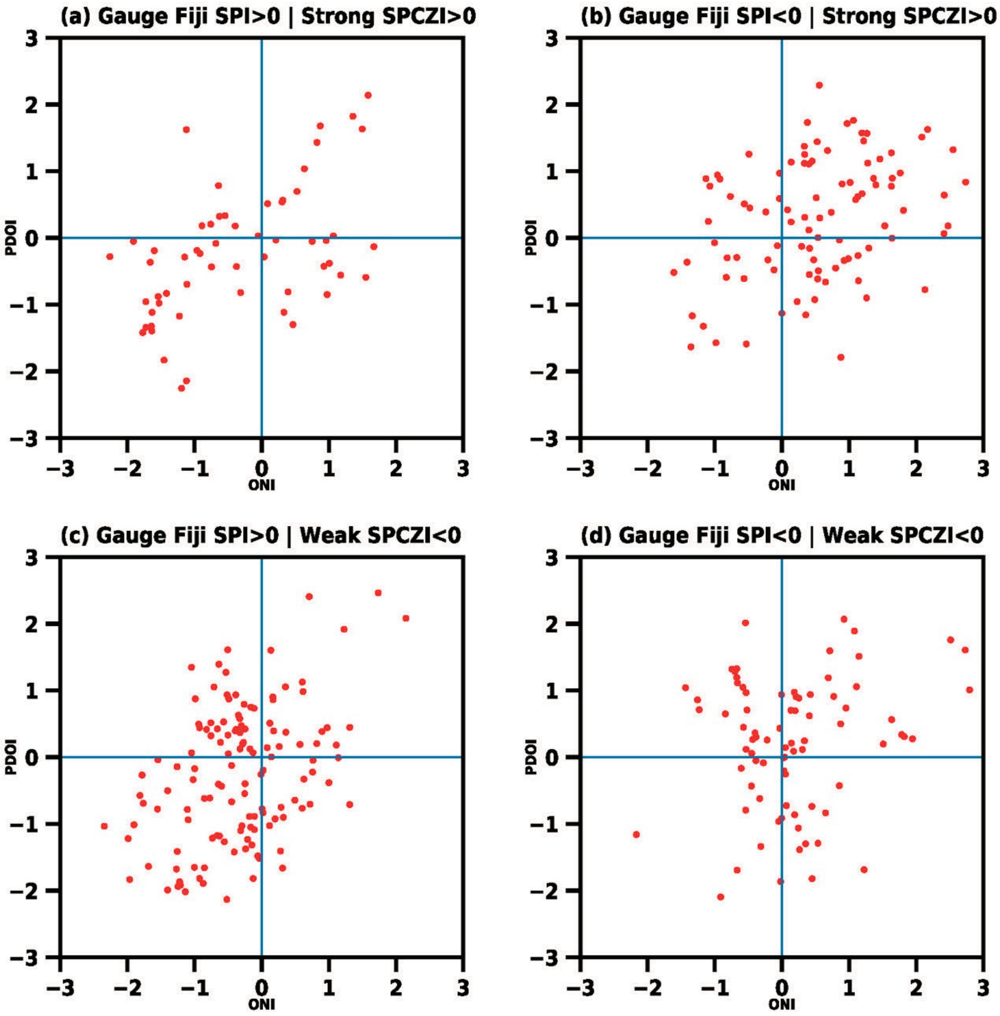

Figure 13. Distribution of wet and dry events in Fiji as a function of ENSO and PDO indices conditional on the strong and weak modes of SPCZ, where: (a) and (c) are for Fiji wet events; (b) and (d) are for Fiji dry events. The wet or dry event was determined by the mean of SPIs at the four gauges.

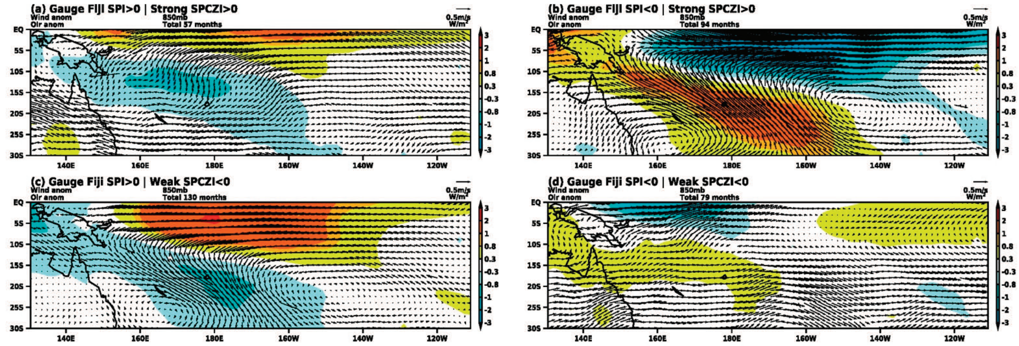

Figure 14. Composite of OLR and 850 mb u and v classified by wet and dry conditions over Fiji and strong and weak modes of SPCZ. OLR, u, v, and SPCZ modes were derived from the ERA-Interim. SPI is the averaged SPI derived from rainfall at the four gauges.

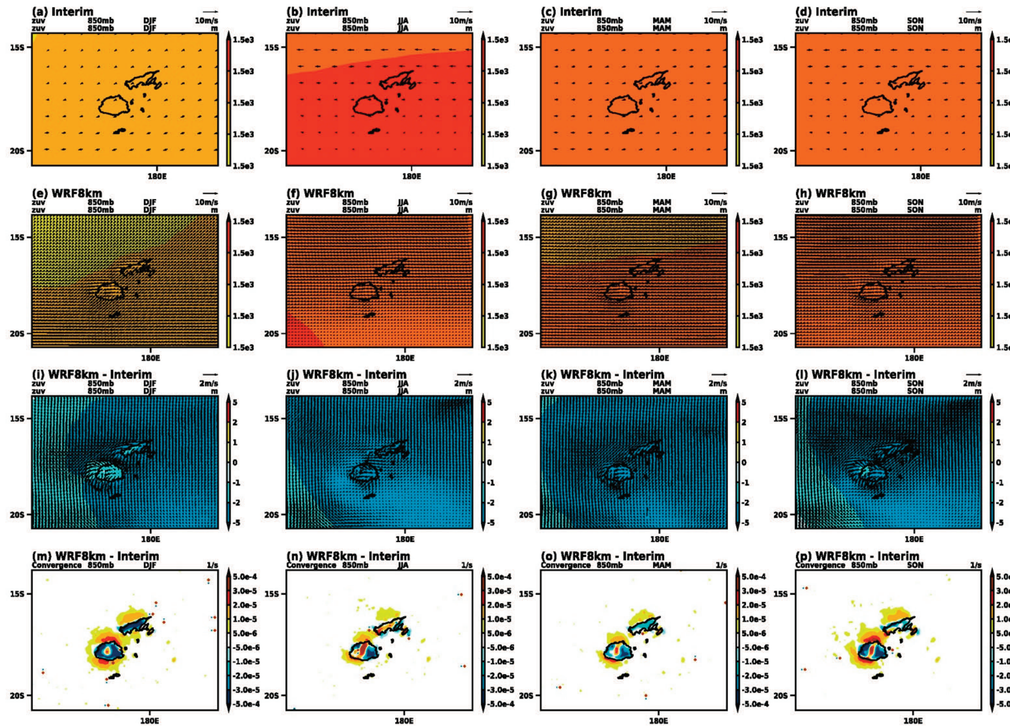

Figure 15. Climatological low-level circulation of the ERA-Interim (a,b,c,d), WRF_8km experiment (e,f,g,h), their difference (i,j,k,l), and the difference of low-level convergence (m,n,o,p) in four seasons between 1981 to 2010.

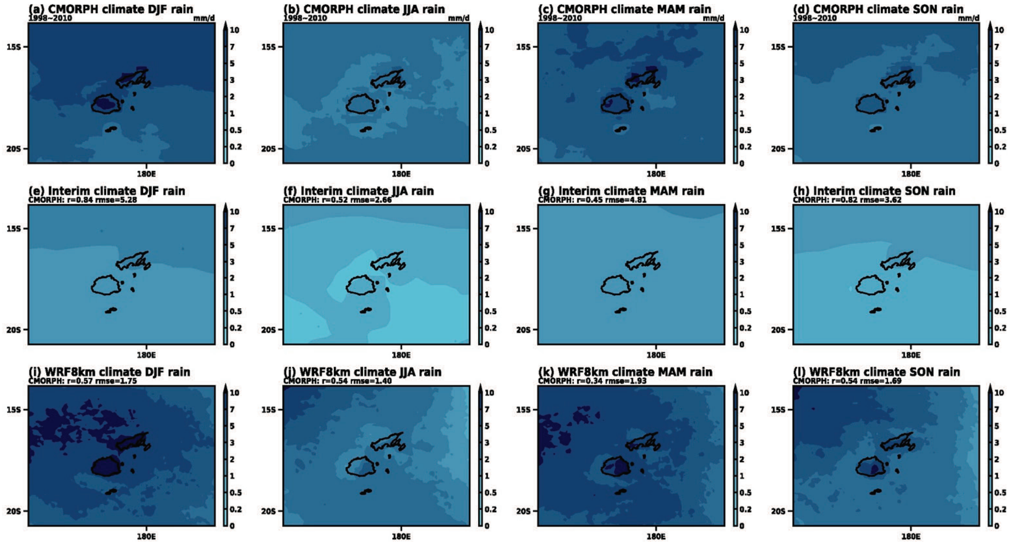

Figure 16. Climatological rainfall of CMORPH (a,b,c,d), the ERA-Interim (e,f,g,h), and WRF_8km simulation (i,j,k,l) in four seasons.

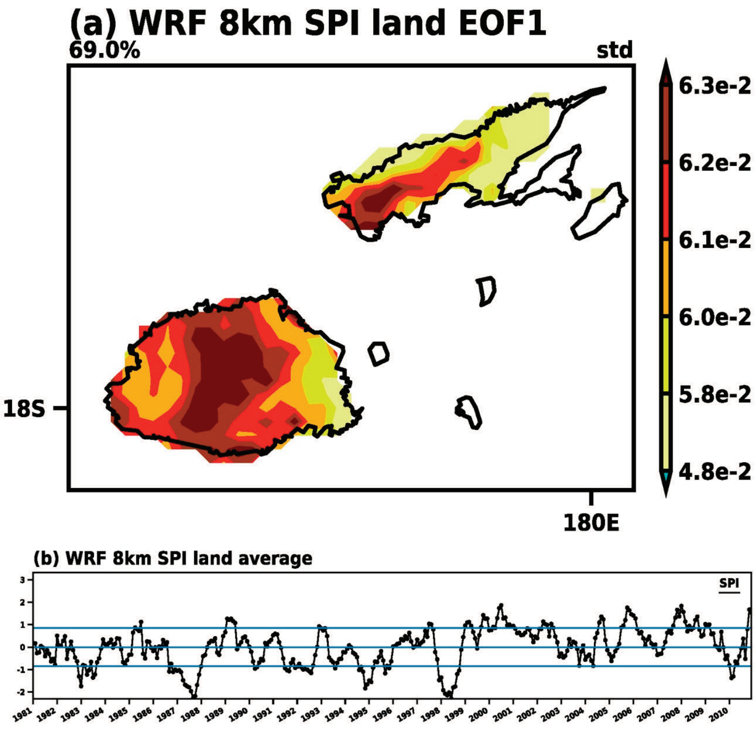

Figure 17. The first EOF mode (a) and the corresponding principal component (b) of SPI derived from rainfall simulated in the experiment of WRF_8km over Viti Levu and Vanua Levu.

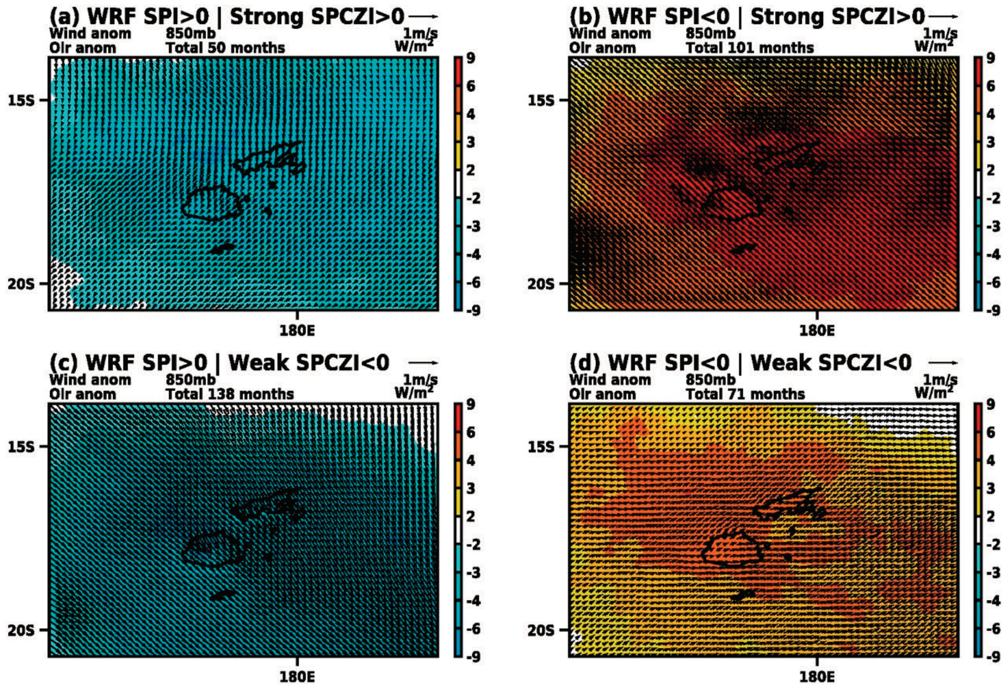

Figure 18. Composite of OLR and 850 mb u and v classified by wet and dry conditions over Fiji and strong and weak modes of SPCZ. OLR, u, v and SPI were obtained from downscaling of the WRF_8km experiment. The SPCZ strength index was derived from the ERA-Interim

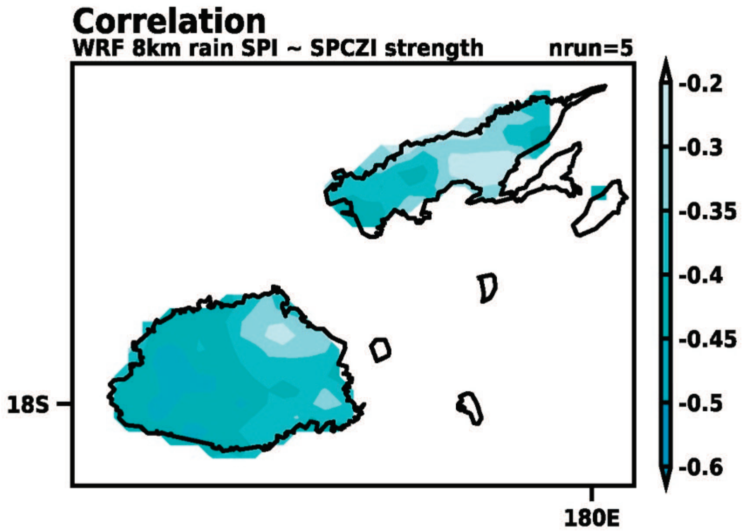

Figure 19. Correlation between the SPCZ index and model grid SPI derived from the downscaled rainfall data.

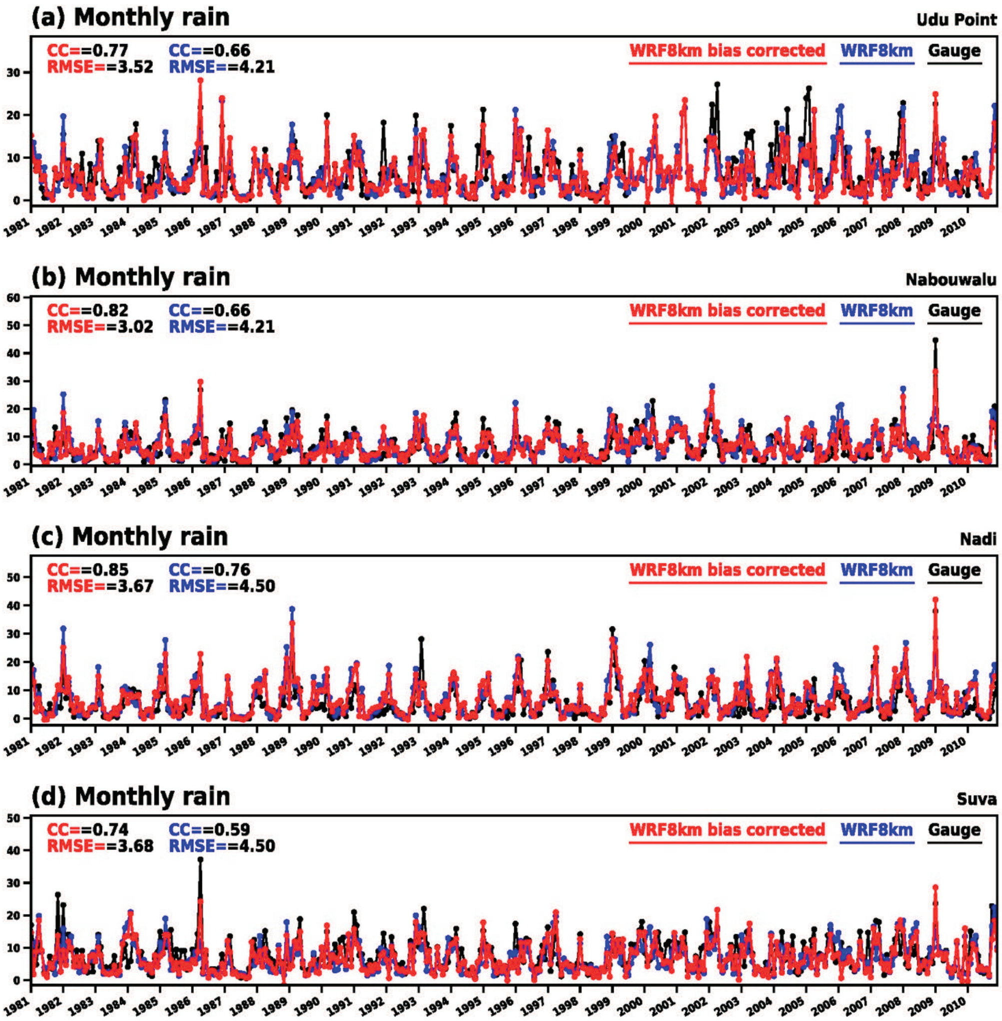

Figure 20. Comparison of rainfall and the bias-corrected rainfall at the four gauges.

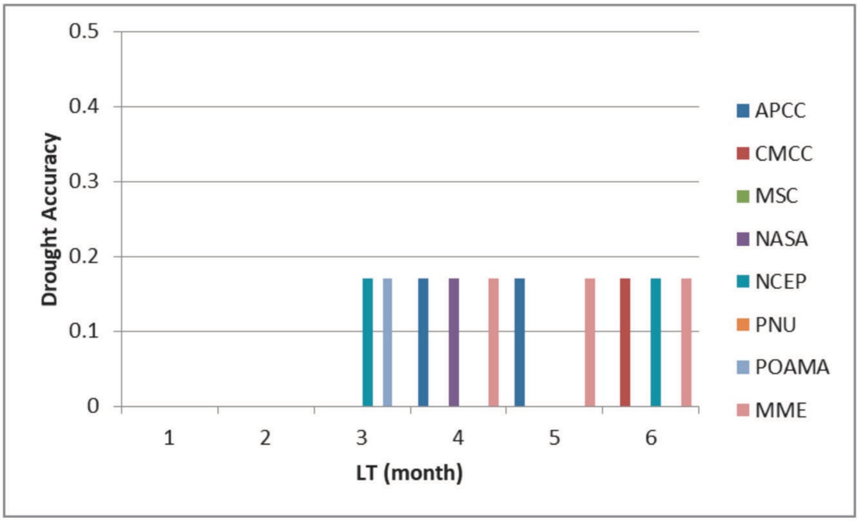

Figure 21. Drought Accuracy of FCST_ONLY cases with reference data of SPI6_OBS from in-situ data.

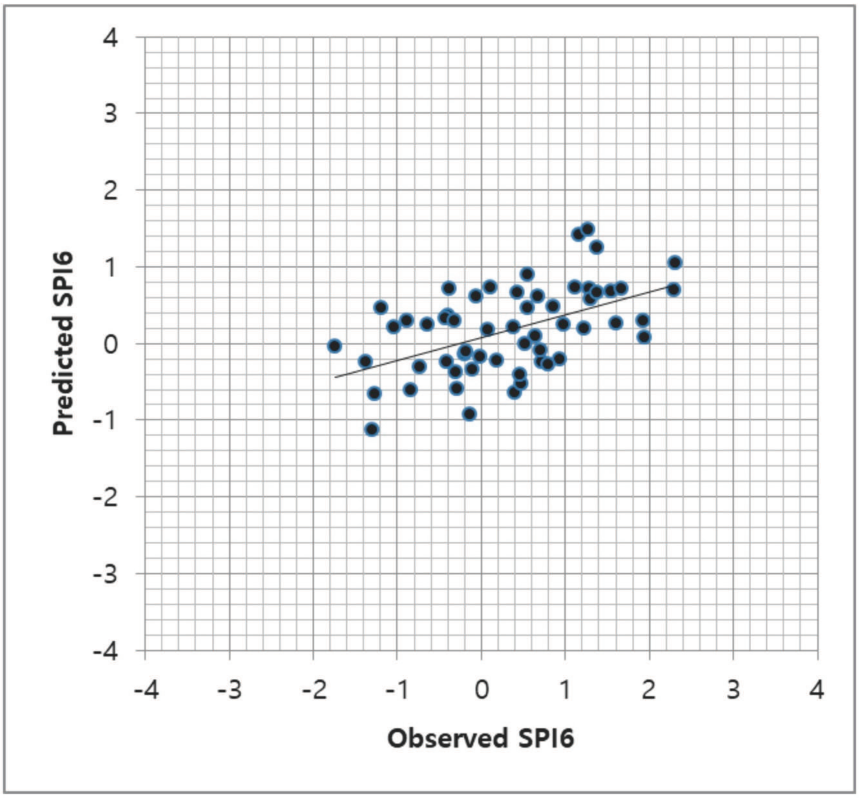

Figure 22. Scatter plot of observed vs. predicted SPI6 for the FCST_ONLY method with climate model MME, with 4-month lead-time and reference data of SPI6_OBS from in-situ data.

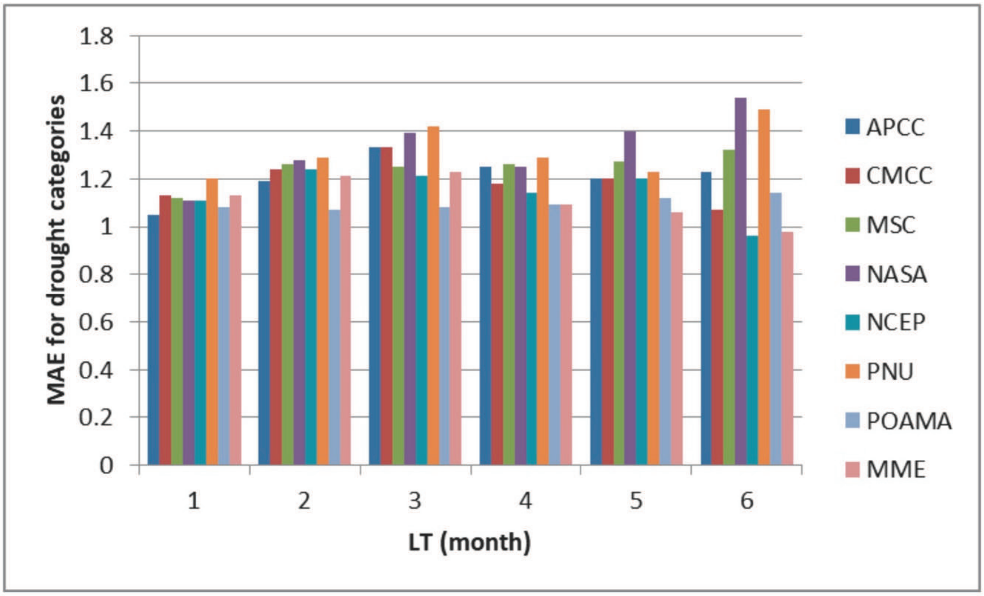

Figure 23. MAE for drought categories of FCST_ONLY cases with reference data of SPI6_OBS from in-situ data.

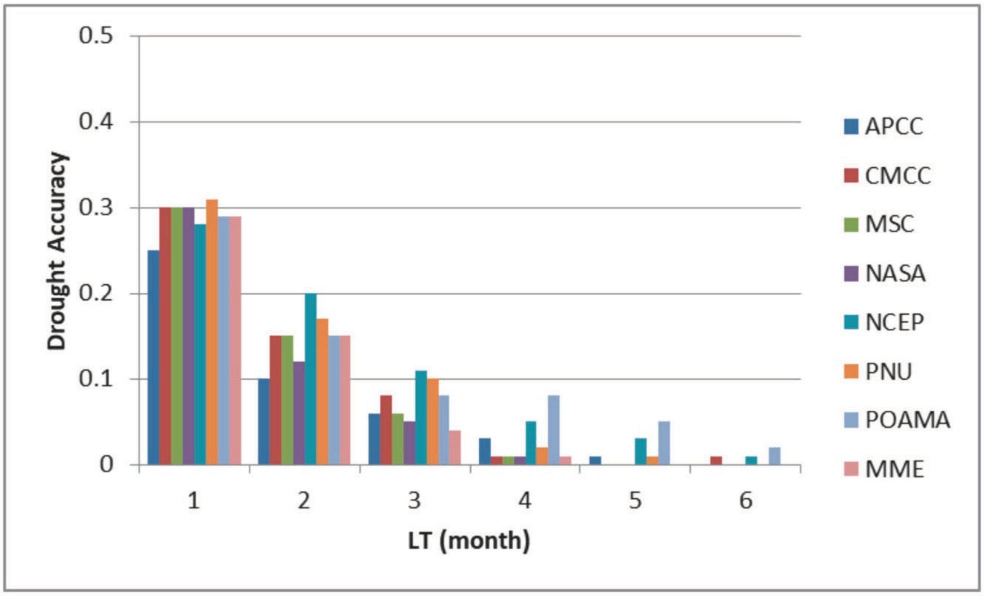

Figure 24. Drought Accuracy of FCST_ONLY cases with reference data of SPI6_OBS from the WRF model outputs.

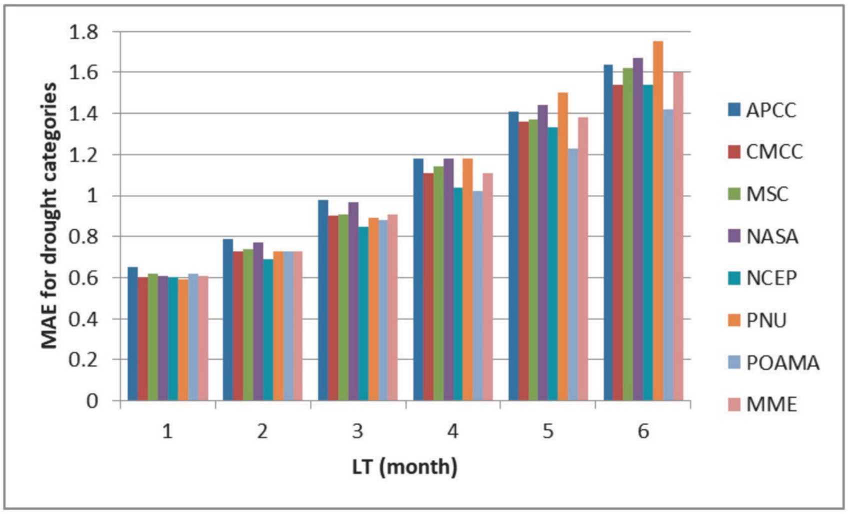

Figure 25. MAE for drought categories of FCST_ONLY cases with reference data of SPI6_OBS from the WRF model outputs.

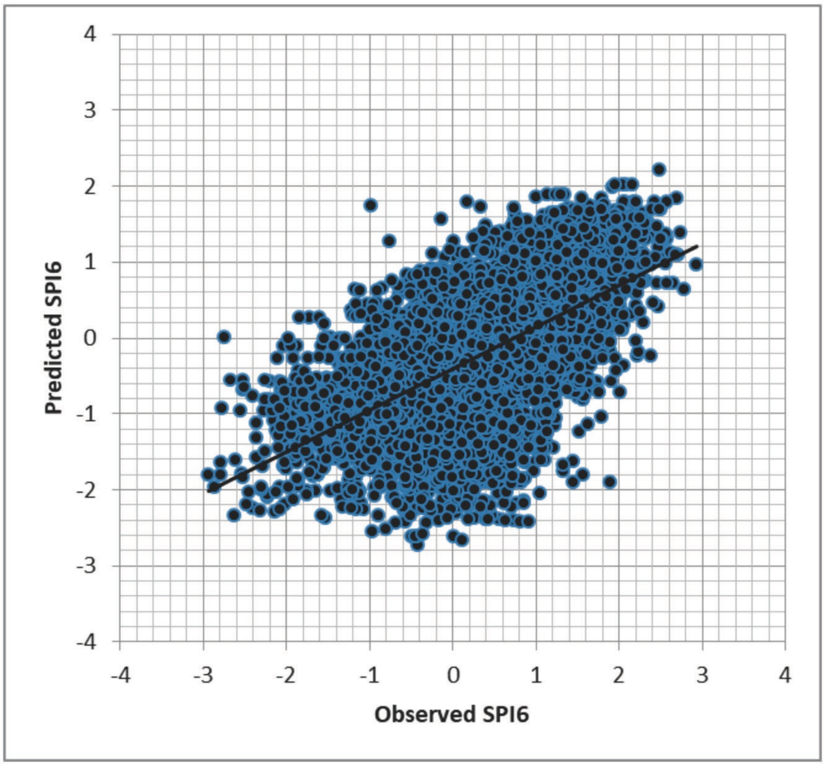

Figure 26. Scatter plot of observed vs. predicted SPI6 for FCST_ONLY with climate model PNU, with a 1-month lead-time and SPI6_OBS from the WRF model outputs.

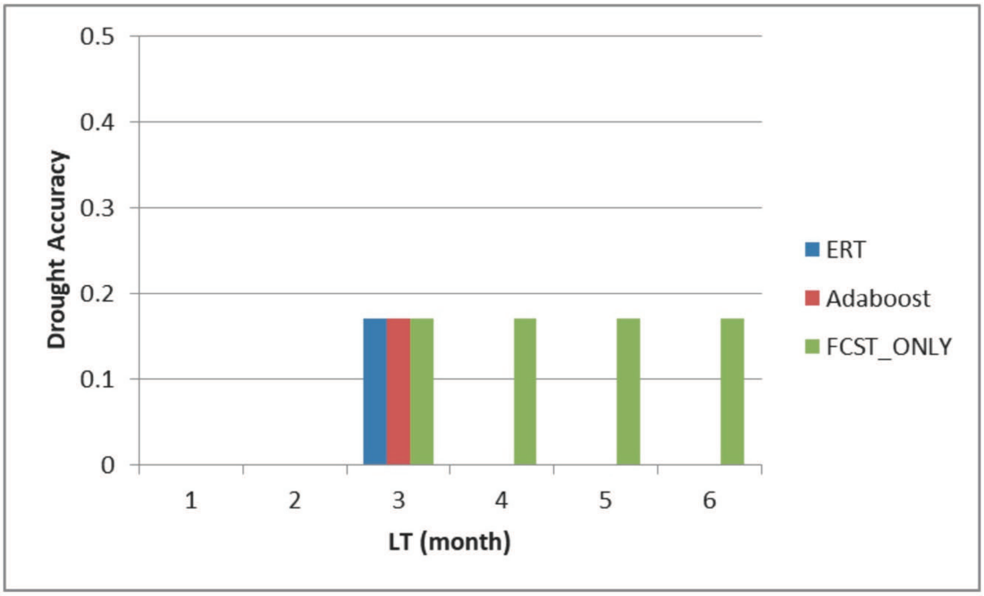

Figure 27. Drought Accuracy of the ERT, Adaboost, and FCST_ONLY models with reference data of SPI6_OBS from in-situ data.

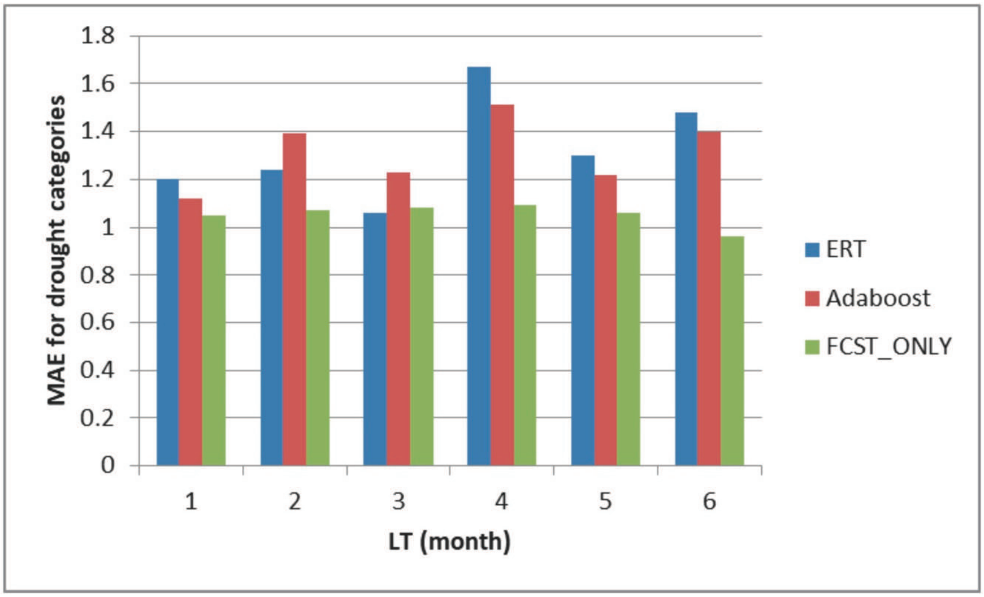

Figure 28. MAE for drought categories of ERT, Adaboost, and FCST_ONLY models with reference data of SPI6_OBS from in-situ data.

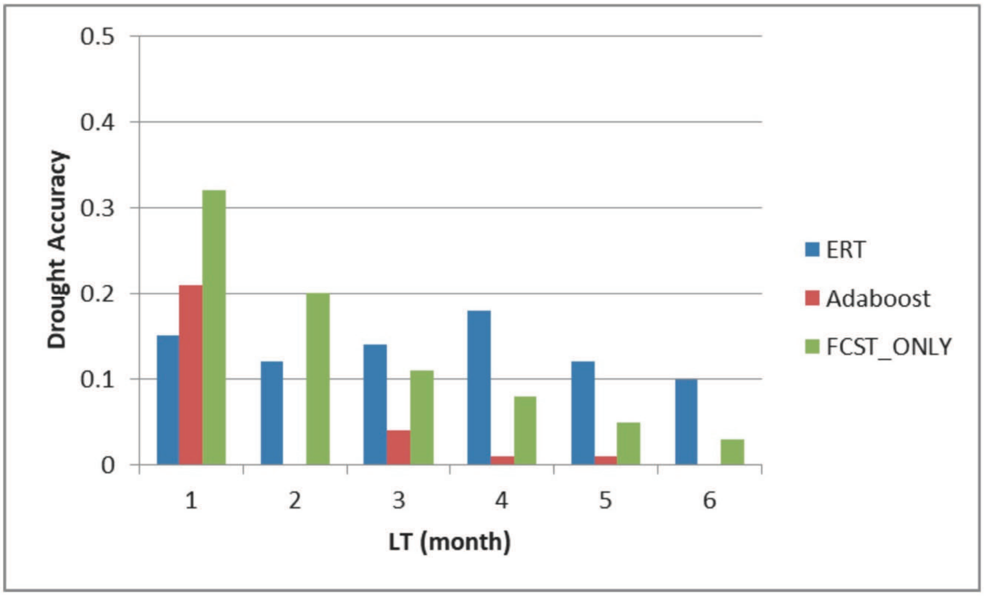

Figure 29. Drought Accuracy of ERT, Adaboost, and FCST_ONLY models with reference data of SPI6_OBS from the WRF model outputs.

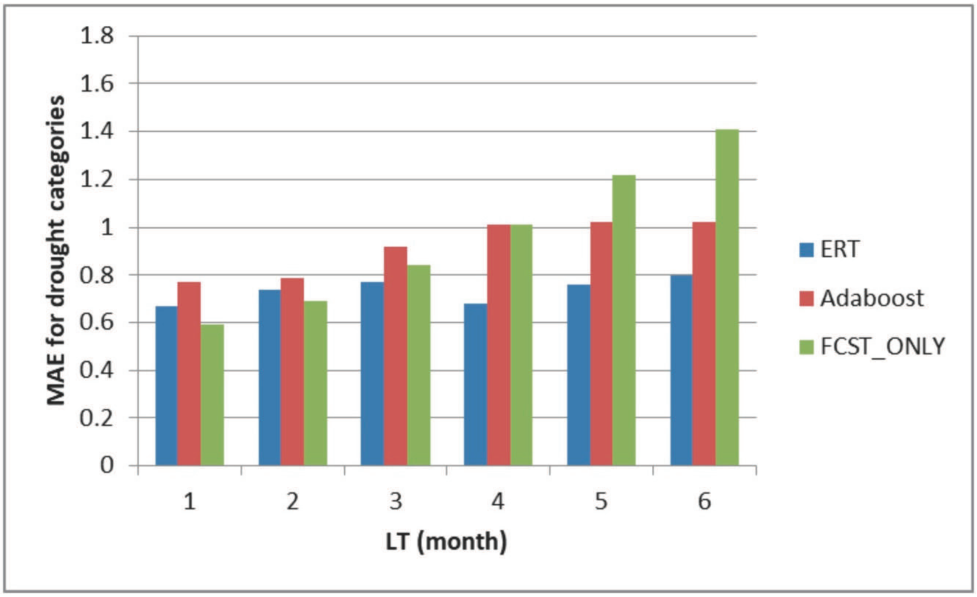

Figure 30. MAE of drought categories of ERT, Adaboost, and FCST_ONLY models with reference data of SPI6_OBS from the WRF model outputs.

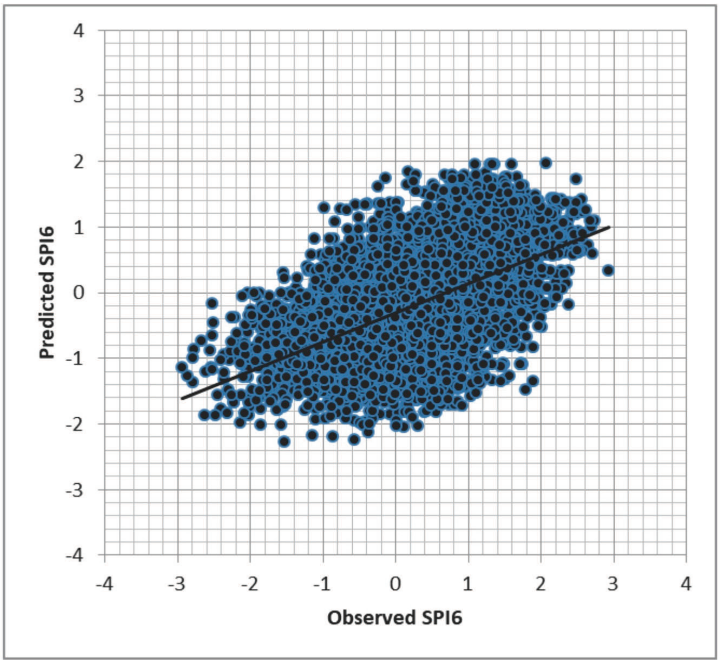

Figure 31. Scatter plot of observed vs. predicted SPI6 for FCST_ONLY with climate model NCEP, with a 2-month lead-time and SPI6_OBS from the WRF model outputs.

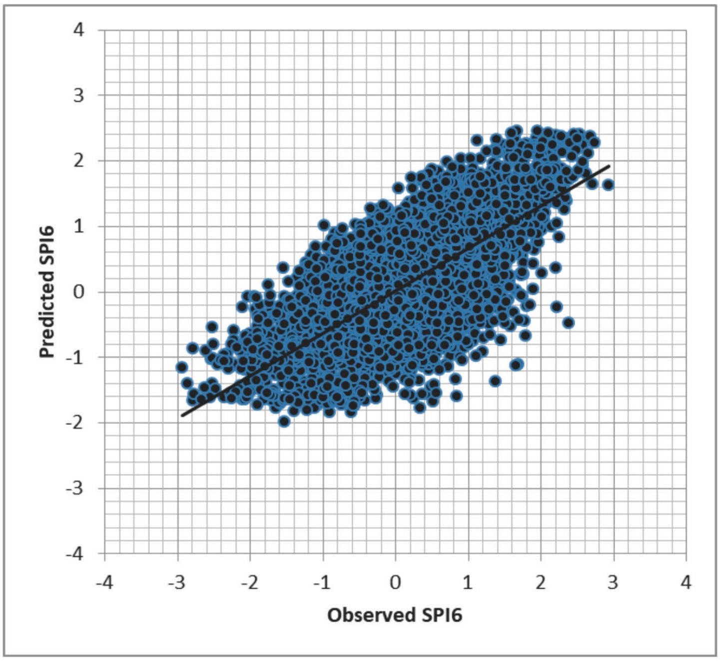

Figure 32. Scatter plot of observed vs. predicted SPI6 for ERT with climate model PNU, with a 2-month lead-time and SPI6_OBS from the WRF model outputs.

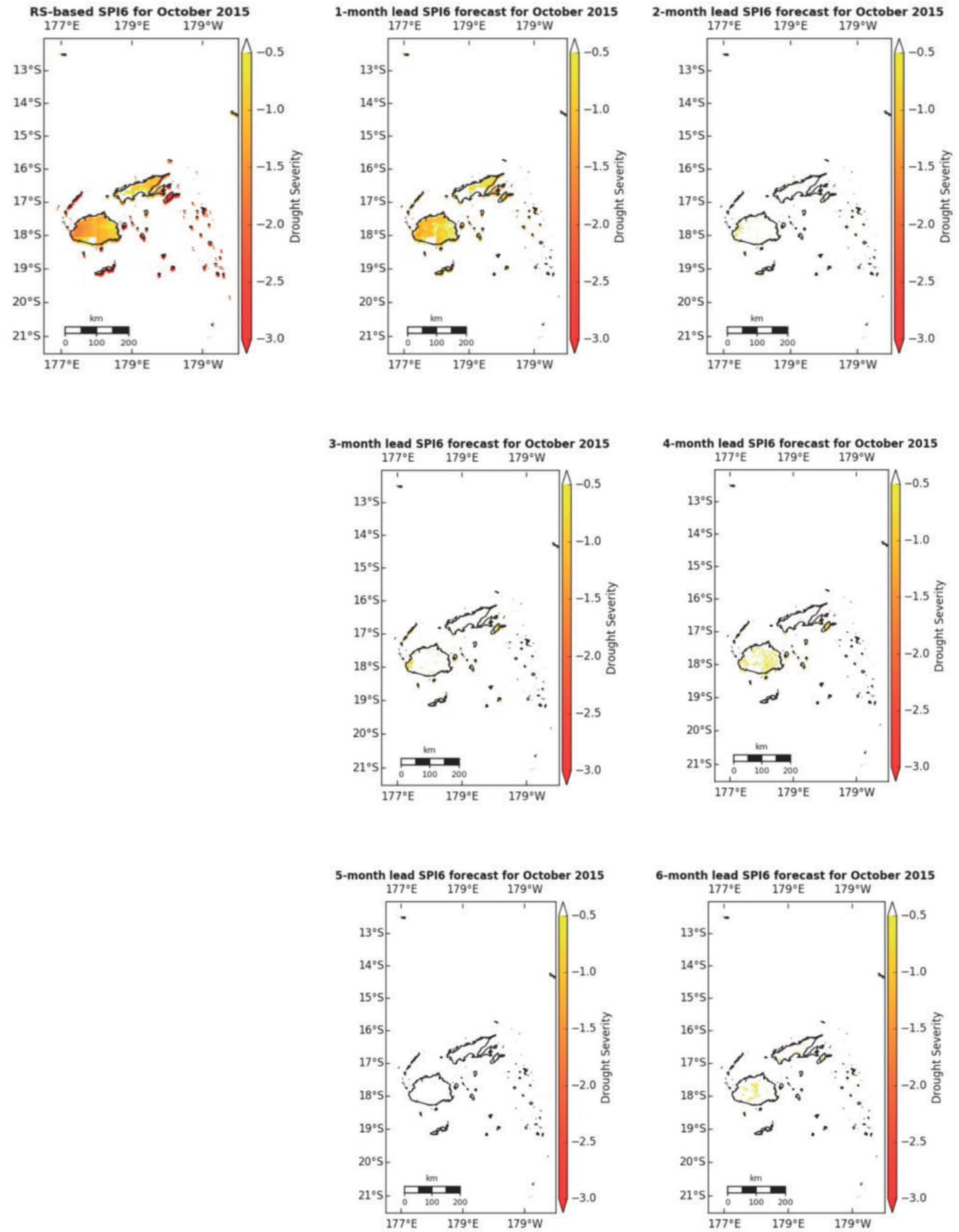

Figure 33. Spatial distribution maps of drought forecasts for October 2015 with 1- to 6-month lead times and remote sensing based SPI6.

【Research Team】

Jinyoung Rhee, Research Fellow

Hongwei Yang, Research Fellow

Research Report 2017-04

Development of a Drought Forecast Model for Fiji based on High-Resolution Dynamic Downscaling of Climate Data and Machine Learning of Long-Range Climate Forecast and Remote Sensing Data

ISBN : 979-11-5698-194-7

Published in March 2018

Published by the APEC Climate Center

Produced by Kyungsung Media